Computational Studies to Understand Nitrile Imine Reactivity in Photocrosslinking to Peptides in Gas-Phase Ions

Tuan Ngoc Kim Vu

A thesis

submitted in partial fulfillment of the

requirements for the degree of

Master of Science in Applied Chemical Science and Technology

University of Washington

2024

Committee:

František Tureček

Robert E. Synovec

Program Authorized to Offer Degree:

Department of Chemistry

University of Washington

Abstract

Computational Studies to Understand

Nitrile Imine Reactivity in Photocrosslinking to Peptides in Gas-Phase Ions

Tuan Ngoc Kim Vu

Chair of the Supervisory Committee:
František Tureček
Department of Chemistry

Computational methods were applied to explore the behavior of nitrile imines as photocross-linkers in gas-phase peptide ions. Irradiating peptide-2,5-diaryltetrazole conjugates (peptide-*tet*) at 250 and 213 nm yielded nitrile imines, which crosslinked with amide carbonyl and side-chain groups in the peptides. Structural and compositional analysis of crosslinked products was conducted using collision-induced dissociation (CID), ultraviolet photodissociation (UVPD) tandem mass spectrometry, and cyclic ion mobility mass spectrometry (c-IMS). Photodissociation tandem mass spectrometry was studied at two wavelengths to probe the energetics of nitrile-imine intermediate formation and its effect on crosslinking. Theoretical calculations were performed using Born-Oppenheimer molecular dynamics for conformational

analysis and density-functional theory (DFT) to evaluate isomer energies. Ion trajectory methods were used to calculate collision cross sections (CCS) of precursors and potential intermediates. Integrating computational data with experimental mass spectra and c-IMS measurements provided a comprehensive understanding of nitrile imine's role as a peptide photocrosslinker in gas-phase ions.

ACKNOWLEDGEMENTS

I am deeply grateful to the individuals whose unwavering support, guidance, and contributions have been indispensable in the completion of this master thesis. At the forefront of my gratitude is Prof. Frantisek Turecek, my PI and my dearest mentor. His mentorship, encouragement, and scholarly insights have profoundly influenced this work. Frank's dedication to excellence, intellectual generosity, and profound understanding of the subject matter have not only shaped the direction of this thesis but have also significantly enriched my academic journey. His encouragement to believe in myself and my capabilities has been transformative, empowering me to overcome challenges and pursue ambitious research goals. Without his guidance and encouragement, I would not have had the confidence to embark on this journey or navigate its complexities with resilience and determination. I can write more and more, but I'll stop here. Thank you so much Frank, from the bottom of my heart.

I want to give a big shoutout to Dr. Martin Sadilek, our department mass spec technician who's been an absolute legend throughout this journey. Martin's not just your typical lab member; he's the one with the best jokes and the uncanny ability to fix any instrument glitch in a heartbeat. His laid-back vibe and technical wizardry made our lab feel like home, even during the most stressful experiments. Massive thanks to Martin for always having our backs and keeping the lab vibes positive,

Shout out to all the members in Turecek group. I cannot believe we have been together for 2 years. Tons of memories were created and will always be treasured deep down in my heart. To Vaclav, although we had been working together for a few months, all your nice words to me

are really appreciated. To Mikulas, thanks for working together in the same computation project in my last quarters at UW. It'd been great to know you and wish you all the best. To Jiahao, our dear Bo laoshi, thank you so much for everything, both for instruments and all the computational tasks. Thank you so much with your patience to tons of my questions and all out-of-nowhere problems. To Mars and Henry, I'm always amazed with how talented you guys are. You are both doing great with your PhD journey and beyond. To Anatasia, thank you so much for bearing with all my computation instructions. I cannot ask for a better mentee. To Hongyi, my dear mentor and then my dear friend, thank you so much for the last 2 years. You cannot imagine how much I learnt from you.

I would like to thank my family for their continual support in all of my endeavors in life. From my dearest parents, *bố* and *mẹ*, whom encouraged my curiosity in the natural world, believe in my abilities and have been a constant of support unconditionally through all aspects of my life. I thank my brother, *Tô*, for always having managed to tolerate all my nonsense in the last 2 years and helping me with most of the household choirs. Finally, I would like to thank my husband, *Hưng,* who we have been together for 8 years and keep counting. I would not have been able to do it without his support.

DEDICATION

To my dearest MOM and DAD.

TABLE OF CONTENTS

LIST OF FIGURES

LIST OF TABLES

Chapter 1. INTRODUCTION

1.1 CHEMICAL CROSSLINKING AND MASS SPECTROMETRY

Chemical crosslinking is the process of forming covalent bonds between two or more molecules, either intermolecularly or intramolecularly.[1] These bonding agents are known as "crosslinking reagents" or "crosslinkers". They are categorized into various types based on factors such as reactivity and the length of the spacer, each serving specific functions and applications.[2,3] Recently, chemical crosslinking has become a valuable tool for studying biomolecules like proteins.[4] In the biomedical and food packaging industries, a wide range of materials are synthesized utilizing chemical crosslinking methods alongside physical or enzymatic approaches, offering a versatile means to tailor properties such as mechanical strength, biocompatibility, and barrier properties, therefore contributing to the development of advanced biomaterials and sustainable packaging solutions.[1,5,6] These chemical methods employ compounds or crosslinkers sourced from natural origins or synthesized, capable of establishing either covalent or non-covalent bonds with proteins, facilitating linkages through agents such as carbodiimides or epoxides, with the emergence of photo-induced novel chemical crosslinkers offering additional possibilities.[7]

With the advancement in understanding the properties of proteins in the gas phase and ongoing instrument development, both during the transition from solution to gas phase[8] and throughout the flight path within the mass spectrometer,[9] it is increasingly evident that mass spectrometry (MS) has emerged as a cornerstone in the field of structural biology. This technology has revolutionized the capacity to decipher the intricate details of biomolecular

interactions. Taking advantages of MS, cross-linking mass spectrometry (XLMS) has become a resilient and versatile instrument, providing medium - resolution for structure studies.[10]

Analysis of cross-linked peptides by mass spectrometry harnesses several advantages associated with MS analysis.[11] Firstly, the mass of the protein or protein complex being studied is theoretically unlimited, as it is the proteolytic peptides that are analyzed, particularly in cases where a bottom-up strategy is employed. Secondly, MS analysis is generally rapid and requires only femtomole amounts of total protein, even in challenging situations. Additionally, this approach provides insights into the three-dimensional structures of proteins in solution, with flexible regions readily identifiable. Moreover, it is versatile, allowing for the analysis of membrane proteins and proteins existing as mixtures of different species, such as those with post-translational modifications or splice variants. Cross-linking reagents offer a broad range of specificities towards various functional groups like primary amines, sulfhydryls, or carboxylic acids, enabling a wide variety of experimental approaches. Furthermore, MS can provide site specific, low-resolution distance constraints with significantly lower sample quantities compared to NMR or X-ray crystallography, along with faster experimental turnaround times. Finally, MS analysis does not require specific solvents, allowing for in vitro experiments under conditions mimicking native protein environments, which is not feasible with high-resolution techniques like NMR or X-ray crystallography. The recent development of MS-cleavable crosslinkers designed to break in the gas phase during MS^2 analysis has significantly simplified data analysis.

For example, of one of the advantages listed above, MS-cleavable crosslinkers, such as disuccinimidyl sulfoxide (DSSO) and disuccinimidyl dibutyric urea (DSBU), yield two linear peptides containing segments of the crosslinking reagent, distinguishing them from non-crosslinked peptides (as shown in Figure 1.1).[12] By leveraging the MS signature of the cleavable

crosslinker, peptides can be sequenced and identified through MS^3 analysis, facilitating accelerated data processing.

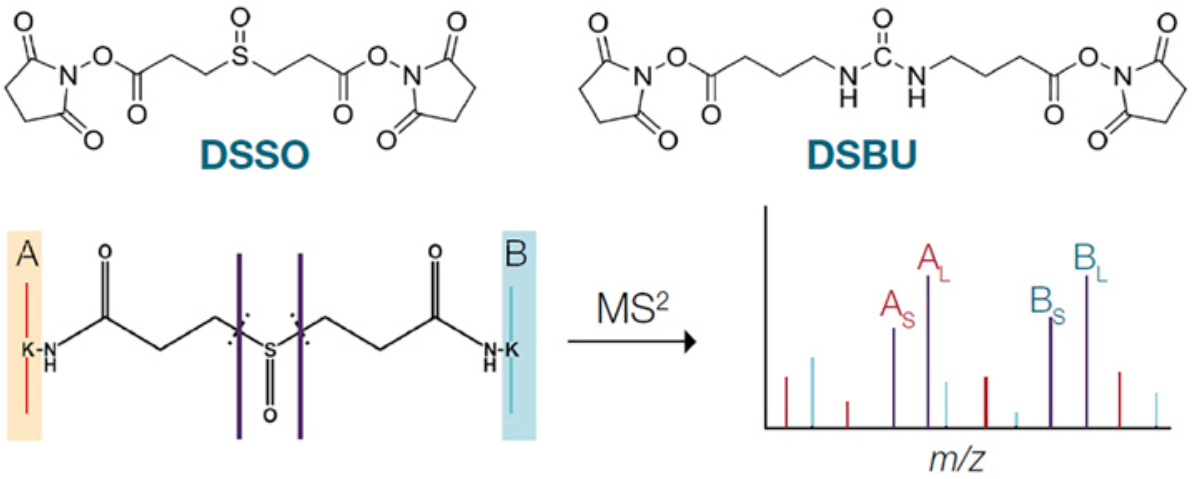

Figure 1. 1. Fragmentation of MS-cleavable crosslinkers by MS^2.[12]

1.2 Photodissociative Cross-Linking in the Gas Phase

The utilization of photochemical crosslinking has been introduced as a novel method for investigating biomolecular structures and dynamics.[11] Photoreactive groups can be activated to react with target molecules by exposure to UV light. Prior to photolysis, photosensitive functional groups have relatively low reactivity. Therefore, highly controlled conditions required experiences can be benefited from utilizing photoreactive cross-linking reagents.[13] Due to that characteristics, photochemical crosslinking is an established method for structure elucidation of protein-protein[13] and protein-nucleic acid complexes.[14,15]

Gas-phase crosslinking is distinguished by several notable features.[16] Firstly, it involves complex formation within electrospray droplets, facilitating library-type screening of crosslinked species. Secondly, the process offers a well-defined stoichiometry of the complexes due to mass-selective isolation, ensuring precise control over the composition of the crosslinked species.

Additionally, gas-phase crosslinking enables facile monitoring of the reaction progress and determination of yield, enhancing experimental efficiency. Furthermore, post-crosslinking structure analysis is achievable through tandem mass spectrometry, which can be complemented by techniques such as hydrogen-deuterium exchange, UV-vis action spectroscopy, and ion mobility measurements, providing comprehensive insights into the structural dynamics of crosslinked biomolecular complexes.

Crosslinking relies on highly reactive intermediates that are transiently produced by photolysis of a stable precursor group (Tag) which is introduced into one component (Probe) of the complex (Figure 1.2). Upon formation, the reactive group (R) undergoes rapid insertion into the sterically accessible X-H bonds in the target component (X = C, N, O), thus forming a covalent bond via a bridging group (L) and converting the complex into a molecule.

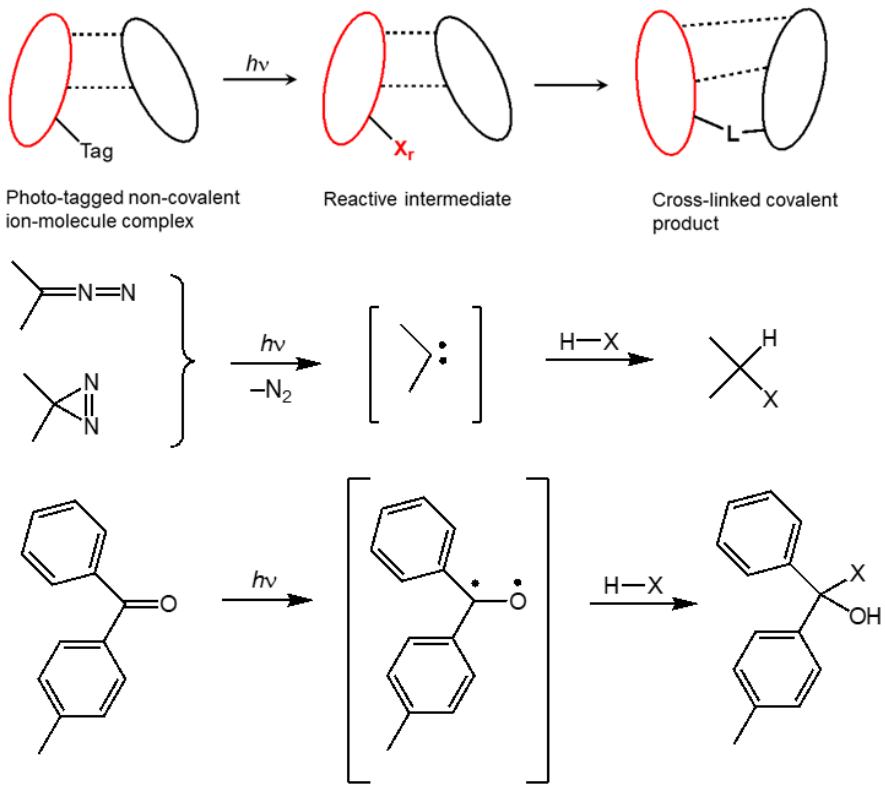

Figure 1. 2. Photodissociative crosslinking.[16]

Westheimer et al.[17] and Knowles and coworkers introduced the concepts of crosslinking and photoaffinity labeling in the 1960s. [18] Reactive intermediates like nitrenes[19] and carbenes,[20,21,] produced through photodissociation, along with triplet states from photoexcitation in benzophenone-tagged proteins,[22-25] have been utilized. Diazirines[26-28] and diazoalkanes,[29] stable sources of carbene, have been extensively employed in studies involving photoaffinity labeling and foot printing of various biomolecules. [21, 30-32] The generation of reactive carbene occurs through photodissociation, for instance, at 350-360 nm from diazirines, which then rapidly reacts with bonds in the target molecule, including addition to double bonds[33] and insertion into C-H bonds. [34,35] Spectroscopic techniques[36,37] such as EPR[38] spectroscopy have aided in product identification, while reaction kinetics have been explored through methods like laser flash photolysis,[39] analysis of kinetic isotope effects,[40] and quantum mechanical tunneling[41] revealing very low activation energies for insertion reactions. [35-37] In parallel, carbene insertion reactions have been used to achieve covalent crosslinking in non-covalent complexes that almost always involved polar compounds, such as peptides, proteins, etc.[11,21] where low activation energies were presumed to facilitate covalent bond formation.

The choice of reactive groups has been limited by the requirement that the precursor is stable and can be incorporated into the complex in a site-specific manner.

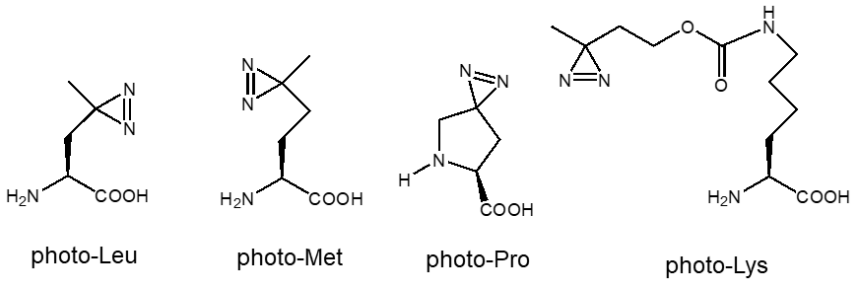

Figure 1. 3. Diazirine-tagged amino acids available commercially.[16]

The Turecek group has introduced photochemical crosslinking in gas-phase peptide-peptide,[41-46] peptide-nucleotide,[47] and peptide-ligand complexes.[48] This has relied on carbene intermediates that were generated by UV-vis photodissociation (UVPD) of diazirine-tagged peptides or ligands.[43] Diazirine photodissociation is readily monitored by mass change in the gas-phase complex ion by N_2 elimination. Crosslinks are analyzed by CID-MS^3 sequencing that allows one to identify the amino acid residues that were targeted by the carbene.[41] This scheme is fundamentally different from other methods of gas-phase covalent bond formation, such as non-selective photodissociation of small peptide complexes at 157 nm,[49] or gas-phase anion-cation reactions of active esters with peptide N-terminus.[50,51] Photoexcitation at 157 nm is inherently nonselective because it does not target a particular chromophore, and thus cannot be used for structure analysis of the complex. Ion-ion reactions do not address non-covalent complexes whereas the interaction between the gas-phase reagents is dominated by strong ion-ion attractive interactions. While carbene-based crosslinking can be considered a general method of wide applicability, it also has inherent limitations. One of those is the very low extinction coefficient for the electronic excitation in the diazirine ring. This involves the dipole forbidden $xy \rightarrow z$ transition[26,27] that has a very low oscillator strength, which adversely affects the photodissociation conversion. Another drawback is the overall indiscriminate carbene reactivity that can attack any proximate X-H bond in the target moiety, which complicates product analysis.

Chapter 2. BACKGROUND

2.1 NITRILE IMINE AS PEPTIDE-PEPTIDE PHOTODISSOCIATIVE CROSSLINKERS

Nitrile imines were discovered by Huisgen *et al.* in 1959.[52] Since then, nitrile imines have become a more and more popular with organic and material chemists due to their broad applicability in the synthesis of biological scaffolds[53] on par with novel synthetic materials.[54] The most common precursors of nitrile imines are hydrazonyl halides and 2,5-diaryltetrazoles.

The use of nitrile imines as peptide-peptide photodissociative crosslinkers represents a cutting-edge approach in mass spectrometry-based structural biology. By harnessing the unique chemical properties of nitrile imines, researchers can selectively and covalently link peptides, providing precise spatial information about their interactions. This methodology finds applications in studying peptide-protein interactions, mapping peptide structures, and investigating conformational changes. As researchers optimize methodologies, tackle computational challenges, and explore new frontiers, the use of nitrile imines as crosslinkers holds great promise in unraveling deeper layers of the structural intricacies governing peptides and their dynamic interactions in biological systems.

Nitrile imines are characterized by the presence of a reactive nitrile group and an imine moiety. The reactive intermediates are known to undergo [3+2] cycloadditions[55] to enones, alkylidene malonates, and a broad range of other dipolarophiles, that have been used in the synthesis of various five-membered heterocyclic systems, as shown in Figure 2.1. [56-61] As reactive intermediates, nitrile imines are readily accessible by photolysis or thermolysis of tetrazoles, base-induced elimination from hydrazonyl halides, and by other methods.[62] 2,5-Diaryltetrazole carboxylates have been used by Song et al. to conjugate the tetrazole group to the lysine -amino group in peptides for further modifications by [3+2] cycloaddition with

dipolarophiles.[63] Despite the broad range of dipolarophiles used for reactions with nitrile imines, there has been paucity of reports of reactions with functional groups pertinent to biomolecules, such as amide groups in proteins and purine and pyrimidine heterocycles in nucleic acids. Chlorinated nitrile imines have been reported to undergo [3+2] cycloaddition to enamides, but addition to an inactivated amide group has not been reported. The electronic properties of nitrile imines have been studied by Wentrup and coworkers.[64,65]

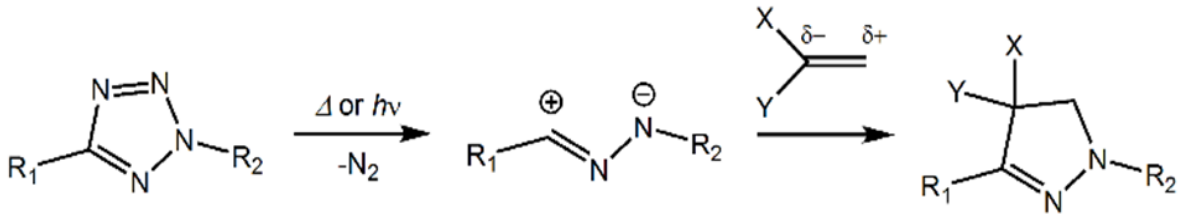

Figure 2. 1. Formation of nitrile imines from tetrazoles and [3+2] addition to dipolarophiles

The photoactivation of nitrile imines is a crucial step in the crosslinking process. Laser irradiation at the appropriate wavelength induces loss of N_2, generating reactive species that facilitate the formation of covalent bonds. The choice of activation wavelength is determined by the specific properties of the nitrile imine used, optimizing the efficiency and specificity of the crosslinking reaction.[66] Nitrile imines exhibit high specificity in their reactivity, contributing to the accuracy of the crosslinking process. This specificity is crucial for selectively capturing interactions between peptides without introducing non-specific crosslinks, enhancing the reliability of the structural information obtained. The calculated reaction enthalpy indicates that photodissociation at 250 nm, providing photons with 4.96 eV (479 kJ mol^{-1}) energy, is more than sufficient to break the tetrazole ring. As opposed to reactions in the condensed phase, the energy excess in the nitrile imine formation, $\Delta H_{exc} = 479 - 80 = 399$ kJ mol^{-1}, is temporarily stored in

the gas-phase ion because of slow collisional cooling[67,68] and can be used to drive further reactions with proximate functional groups.

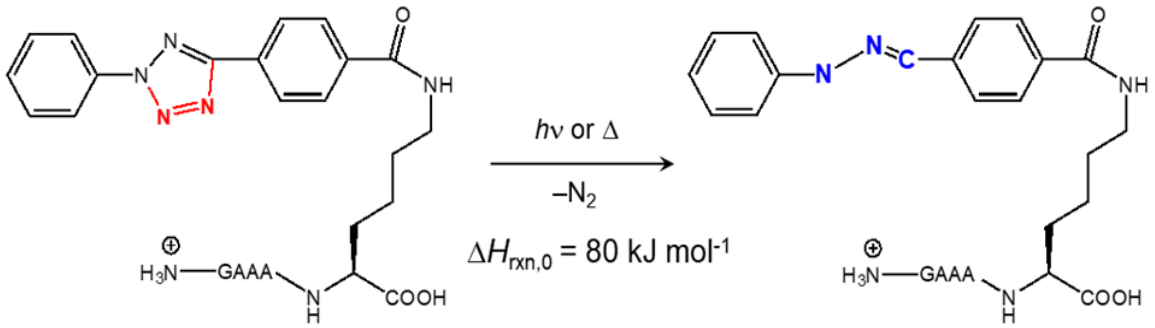

Figure 2. 2. Nitrile imine thermochemistry

2.2 Applied Computational Methods

To further exploit the advantages of nitrile imines as a peptide-peptide photodissociative crosslinkers, I have applied computational methods to investigate ion structures, and crosslinking reaction mechanisms and dynamics at the molecular level. This allows for a deeper understanding of how crosslinking occurs and how it impacts the properties and behavior of the resulting materials or molecules.

Ion structures were obtained by a multistep procedure shown in Figure 2.3. Briefly, several conformers were generated by Born-Oppenheimer molecular dynamics (BOMD) calculations of 20 ps trajectories with 1 fs steps that was performed by PM6-D3H4.[69] These calculations were run under the high-level Cuby4 platform,[70] developed by Řezáč, with the Berendsen thermostat algorithm.[71] PM6 calculations were run under MOPAC.[72] It should be noted that because both electron and nuclear motions are treated explicitly by BOMD, the initial proton positions are not fixed and protons can move among accessible positions in the course of

the trajectory calculations. Two hundred snapshots of each trajectory were taken at regular intervals and fully gradient-optimized with the all-valence-electron semi-empirical PM6-D3H4 method, that captures hydrogen bonds and dispersion interactions in the complexes.

In the next step along this computational process, multiple selected complex structures are fully optimized by density functional theory (DFT) methods and ranked by their relative Gibbs energies. In more details, the resulting structure set from BOMD and PM6-D3H4 calculations were compacted by removing duplicates and submitted to gradient geometry optimization with B3LYP hybrid density functional[73] that was augmented by empirical dispersion terms[74] with Becke-Johnson damping (GD3-BJ).[75] for smooth convergence of geometry and energy. This provided several structures for each protomer that were characterized by harmonic frequency calculations, that were used to evaluate enthalpies, entropies, and thermal free-energy corrections, as local energy minima.

Additional sets of B3LYP optimized geometries were obtained by M06-2X calculations[76] with the 6-31+G(d,p) basis set that were also used for single-point energy calculations with M06-2X/6-311++G(2d,p). This is natural for M06-2X/6-311++G(2d,p) single-point energy calculations, where triple-ζ quality basis sets improve accuracy and were used by Zhao and Truhlar to benchmark the density functional.[76] Charge distributions were calculated according to Merz, Singh and Kollman (MK) scheme.[77,78] Collisional cross sections were calculated by the modified ion trajectory method (MobCalMPI),[79,80] package of Ieritano, Hopkins et al., using the MK charge densities. The experimental localization of crosslinked regions and CCS data along with computational structure and energy analysis represent a powerful approach that allows one to achieve de novo structure assignments for ion complexes. Excited states were calculated by time-dependent density functional theory[81] using M06-2X/6-31+G(d,p). Typically, 15-20 excited

states were considered. Vibronic absorption spectra were calculated for electronic excitations from 300 Wigner configurations[82,83] that were generated from B3LYP vibrational frequencies and sorted out by their Boltzmann factors. These calculations were run using the NewtonX software.[84]

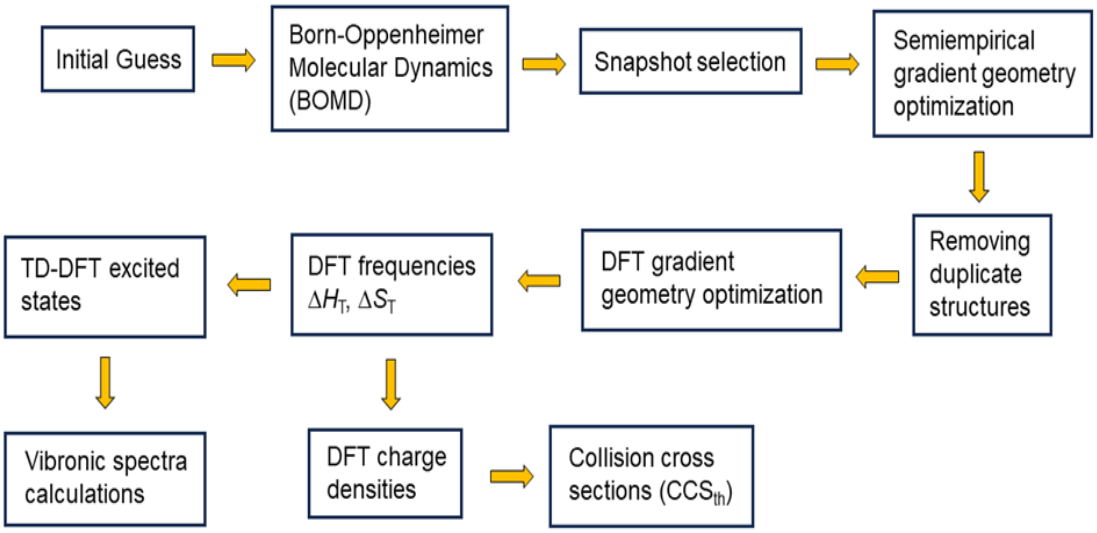

Figure 2. 3. Workflow of BOMD and density functional theory calculations of structures, excited states, vibronic spectra, and collision cross sections.

Chapter 3. COMPUTATION INVESTIGATION OF NITRILE IMINES IN GAS-PHASE IONS

3.1 GAS-PHASE PEPTIDE IONS

The effect on nitrile imine formation and dissociations of modifying the C-terminus and N-terminal amino acid residues in the peptide-*tet* conjugates had been investigated. Modifications of the N-terminal residues such as in (GAAA(*tet*)K + H)$^+$ did not affect UVPD, resulting in an efficient loss of N_2 and nitrile imine formation. Similarly, placing the *tet*-tagged lysine at the N-terminus as in ((*tet*)KAAAG + H)$^+$, resulted in efficient N_2 loss upon UVPD. BOMD and DFT calculations were used to establish theoretical ion structures.

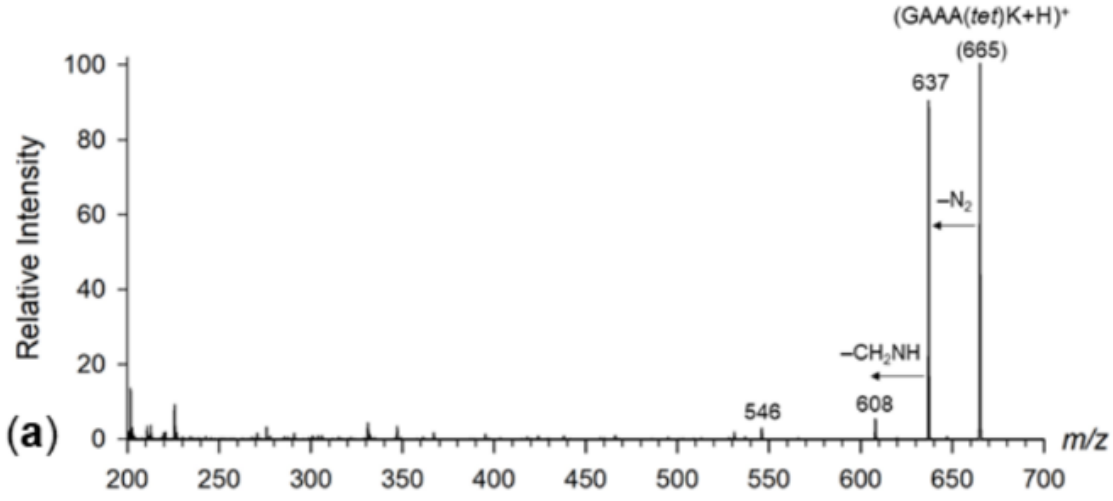

Figure 3. 1. UVPD-MS^2 spectra, 2 laser pulses at 250 nm, of (GAAA(*tet*)K + H)$^+$, m/z 665

3.1.1 *GAAA(tet)K*

With the purpose to understand more about the potential structures of (GAAA*(tet)*K + H)$^+$ in the MS, BOMD and DFT calculations of ion structures were also performed to explore the structures of (GAAA*(tet)*K + H)$^+$ and its photodissociation products in gas phase ions.

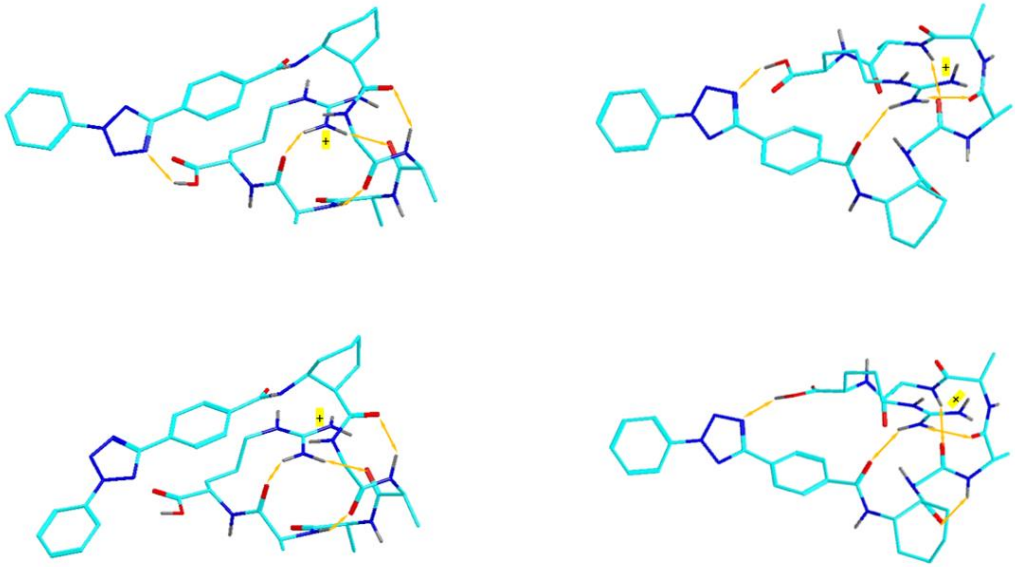

Figure 3. 2. M06-2X/6-31+G(d,p) optimized structures of representative low-energy (GAAA(*tet*)K + H)$^+$ ions

The fundamental question regarding the observed cyclizations in protonated ions was whether they occurred upon the photochemical nitrile imine formation or were promoted by subsequent collisional activation of isolated stable nitrile imine ions. To answer this question, we used action spectroscopy to obtain the UV-vis spectra of the (GAAA(*tet*-N_2)K + H)$^+$ ions. The spectra were obtained in the CID-UVPD mode where the nitrile imine ions used for the action spectra measurements were generated by CID-MS^2 from the tetrazole conjugates. Since CID in the ion trap is performed in a mass-resonant mode, the resulting (peptide(*tet*-N_2) + H)$^+$ ions are not further activated. The action spectrum of (GAAA(*tet*-N_2)K + H)$^+$, which has only a nitrile-imine related chromophore absorbing in the 210-700 nm region, is representative (Figure 3.3).

The action spectrum was monitored for the *m/z* 608 (loss of CH_2=NH, major fragment ion), *m/z* 495 (loss of Ala-Ala), *m/z* 424 (loss of Ala-Ala-Ala), and *m/z* 367 (loss of Gly-Ala-Ala-Ala) photofragment ion channels. The spectrum showed a composite band with maxima at 220, 240, and 250 nm, and another weaker broad band at 270 nm. No absorption was detected above 350 nm.

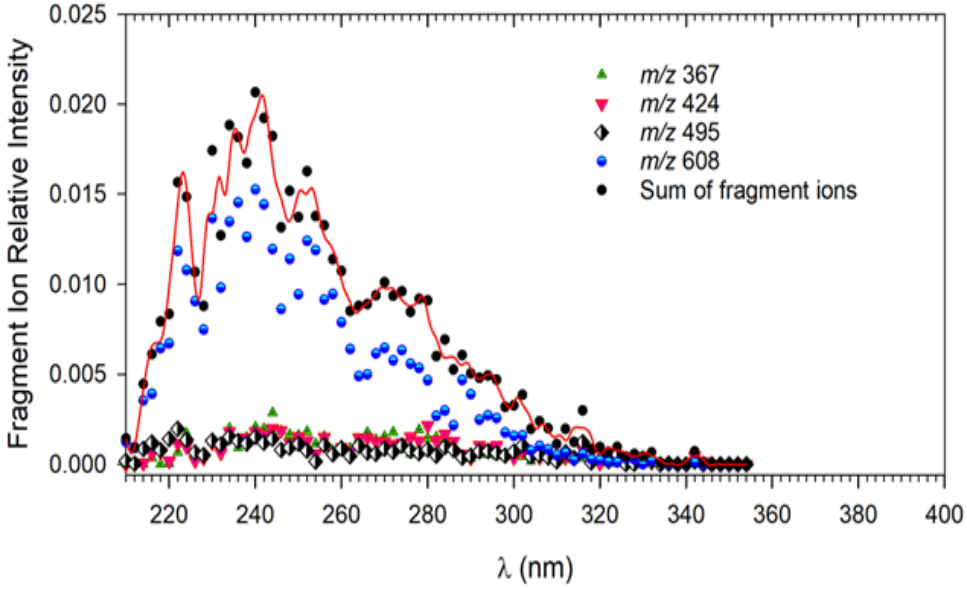

Figure 3. 3. UVPD action spectra of (GAAA(*tet*-N_2)K + H)$^+$

To interpret the spectra and assign the absorption bands, we carried out extensive BOMD DFT calculations of ion structures and excited electronic states for (GAAA(*tet*-N_2)K + H)$^+$. The initial guesses in these calculations were nitrile imine protomers and conformers, as well as cyclized structures involving functional groups that can potentially give rise to the major fragment ions in the CID-MS^3 spectra. These features involved a free neutral or protonated Gly CH_2NH_2 group to account for the loss of CH2=NH, and a retained phenyl-N-N segment for the loss of phenylhydrazine. The lowest-energy structures of each type are shown in Figure 3.4.

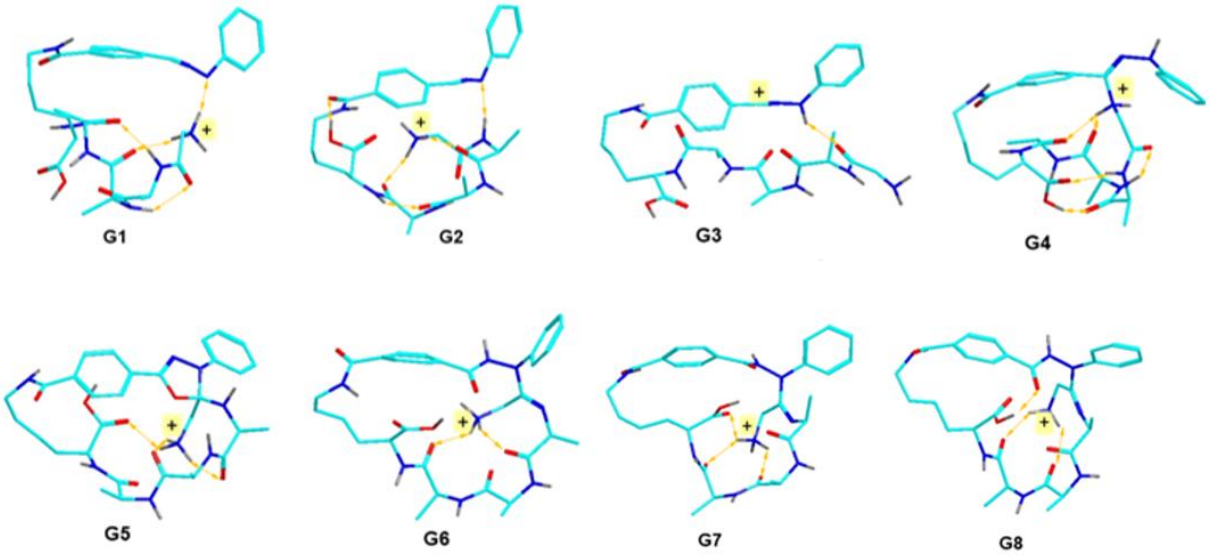

Figure 3. 4. M06-2X/6-31+G(d,p) optimized structures of representative low-energy $(GAAA(tet\text{-}N_2)K + H)^+$ ions **G1**-**G8**. Atom color coding is as follows: cyan = C, blue = N, red = O, gray = H. Only exchangeable hydrogens are shown to avoid clutter. Hydrogen bonds are visualized by double-headed ochre arrows.

For several $(GAAA(tet\text{-}N_2)K + H)^+$ isomers, we also calculated vibronic absorption spectra at 350 K that included excitations from 300 configurations representing the vibrational states of the ions. The low-energy nitrile imines (**G1** and **G2**) showed vibronic spectra that strongly depended on the ion conformation. The lowest-energy conformer **G1** (Figure 3.4) showed a very weak transition to the first excited state at 438 nm (Figure 3.5a). The main transitions at 272, 269, and 246 nm gave rise to the compact band in the vibronic spectrum with a maximum at 270 nm. The other low-energy conformer (**G2**, 13 kJ mol^{-1} relative to **G1**, Table 3.1) showed a strong transition to the second excited state at 290 nm that was spread over a broad range of transitions in the thermal ion reaching beyond 400 nm (Figure 3.5b). Structures produced by simple proton transfer to the nitrile imine group (**G3**, 28 kJ mol^{-1} relative to **G1**)

showed a strong transition to the first excited state at 330 nm (Figure 3.5c) that was incompatible with the action spectrum. The lowest energy structures belonged to hydrazidines (e.g., **G4**, -84 kJ mol^{-1} relative to **G1**) arising by nucleophilic attack at the nitrile imine by the Gly amine group. However, the vibronic spectrum of **G4** showed major bands at 220 nm and an absorption profile that was incompatible with the action spectrum (Figure 3.5d). Oxadiazoles were another type of product that could have arisen by formal [3+2] addition of the Gly amide to the nitrile imine. The lowest energy oxadiazole isomer (**G5**, -68 kJ mol^{-1} relative to **G1**) had a vibronic spectrum that showed a strong transition at 310 nm that resulted in bands at 315 and 345 nm that, however, were absent in the action spectrum (Figure 3.5e).

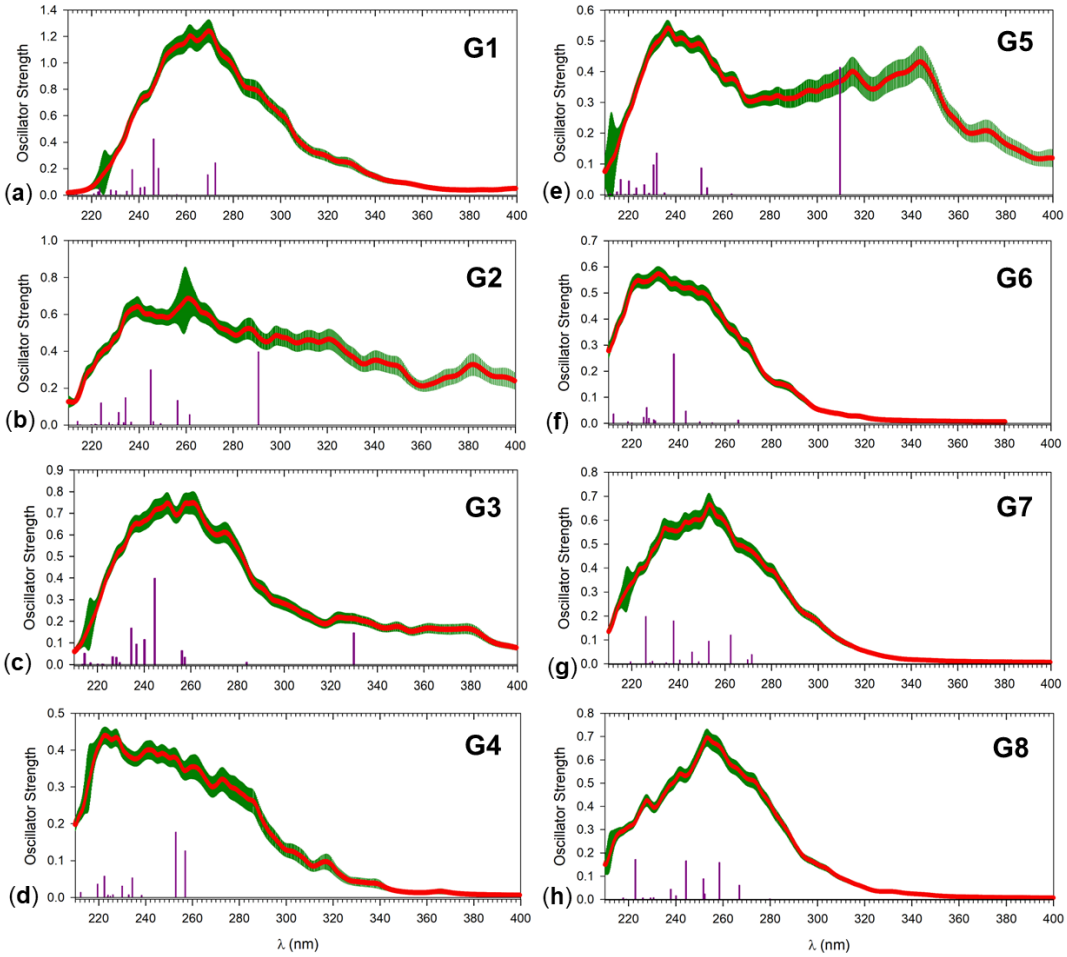

Figure 3. 5. (a)-(h): M06-2X/6-31+G(d,p) vibronic spectra of (GAAA(*tet*-N_2)K + H)$^+$ isomers **G1**-**G8**. Vertical lines represent TD-DFT electron transitions at 0 K. For ion structures, see Figure 3.4.

Since, according to the calculations, the oxadiazole C-O bond in **G5** was weak (ΔH_{rxn} = 24 kJ mol^{-1}), breaking it was considered to be facile. Opening of the oxadiazole ring, followed by proton transfer, formed N-C linked hydrazones that are represented as conformers **G6** and **G7** (-44 and -4 kJ mol^{-1}, respectively, relative to **G1**). The respective vibronic spectra showed bands in the 240-260 nm region (Figure 3.5f,g), and the position of the maxima and the shape of these bands were in good agreement with the bands in the action spectrum. Another low-energy

conformer of this type (**G8**, Figure 3.4) had a vibronic spectrum (Figure 3.5h) that was very similar to those of **G6** and **G7**, illustrating the general features of the diarylhydrazone chromophore. In summary, structures **G1**, and **G6**-**G8** provided the best match with the action spectrum of the $(GAAA(\textit{tet}\text{-}N_2)K + H)^+$ ion.

In an effort to further characterize the ions of interest, we investigated the composition and structures of the peptide tetrazole conjugates and their crosslinked products using cyclic ion mobility spectrometry (c-IMS).[85] This allowed us to separate isomers by their arrival times and obtain collision cross sections (CCS_{exp}) in N_2. $(GAAA(\textit{tet})K + H)^+$ ions showed single peak after five passes (490 cm pathlength) of c-IMS, indicating structurally homogeneous ions (Figure 3.6). The measured CCS_{exp} = 256 $Å^2$ was matched by the calculated CCS_{th} for the lowest Gibbsenergy conformers of these ions (Figure 3.6). The ion was protonated at the *N*-terminus regardless of the initial proton position in structures that were submitted to BOMD. The optimized structures showed globular peptide moieties that were maintained by multiple intramolecular hydrogen bonds. The 2,5-diaryl tetrazole moiety was positioned at the ion periphery and, with the exception of its carbonyl, was not linked by hydrogen bonds to the peptide polar groups. This indicated that the tetrazole group may be viewed as a spectator without significantly affecting the peptide ion conformation. On the other hand, the rigid structure of the 2,5-diaryl tetrazole moiety limits access of the incipient nitrile imine to amide bonds and other functional groups to be located close to the pentapeptide *N*-terminus. From the optimized structures one can assess the minimum number of four residues that separate the tetrazole ring and the incipient nitrile imine from the nearest sterically possible crosslinking site.

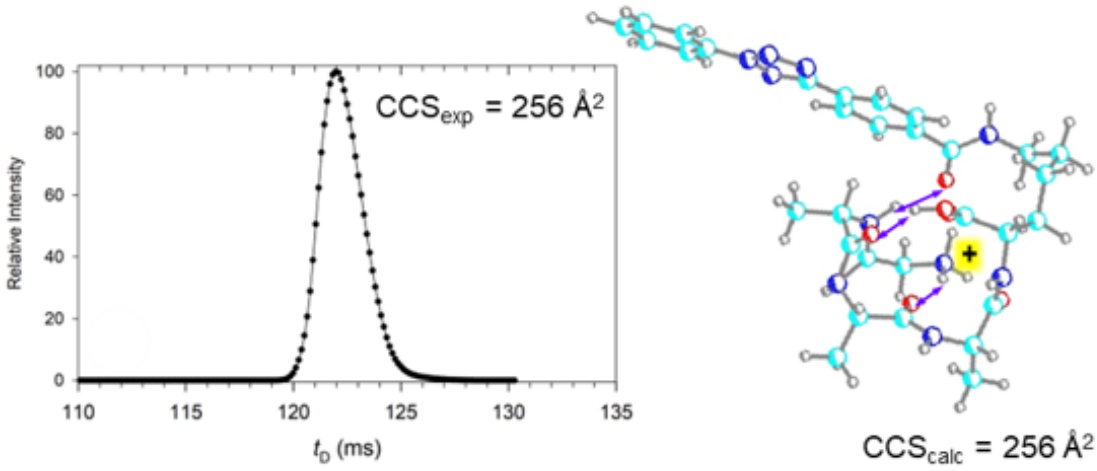

Figure 3. 6. Arrival time profile (5 cycles), optimized structure of (GAAA(*tet*)K + H)$^+$.

In contrast to the precursor ions, the (GAAA(*tet*-N_2)K + H)$^+$ ion generated by CID was mixtures of isomers (Figure 3.7). According to c-IMS, (GAAA(*tet*-N_2)K + H)$^+$ produced two major peaks of CCSexp = 246 Å^2 and 254 Å^2 that were accompanied by two additional minor peaks (Figure 3.7.)

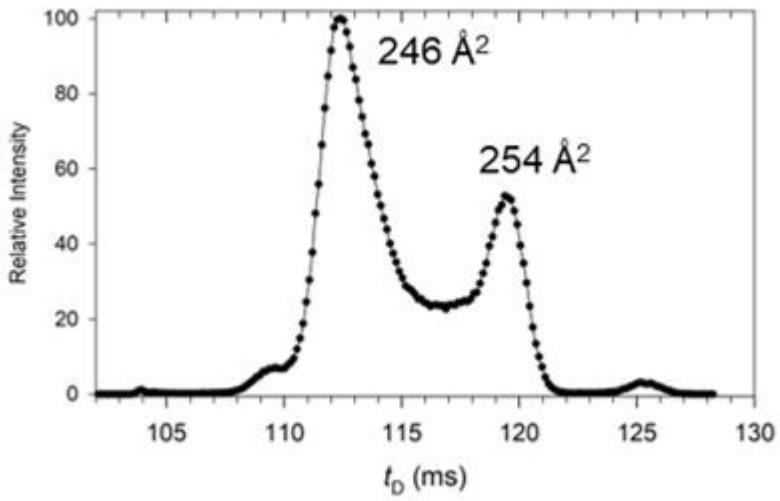

Figure 3. 7. Arrival time distributions after five passes of (GAAA(*tet*-N_2)K + H)$^+$ with experimental CCS$_{exp}$ for the major peaks.

The CCS_{exp} of $(GAAA(tet\text{-}N_2)K + H)^+$ were compared to CCS_{th} that were calculated for several structure types (**G1**-**G8**, Table 3.1). Nitrile imines **G1** and **G2** had CCS_{th} in the 246-250 $Å^2$ range that overlapped with the 246 $Å^2$ peak in Figure 3.7. Considering the minor band at 270 nm in the Figure 3.3 action spectrum that can be attributed to a nitrile imine, the combined data indicated the presence of an unreacted nitrile imine in the mixture. Consistent with this conclusion, the CID-MS^3 spectrum of $(GAAA(tet\text{-}N_2)K + H)^+$ (Figure 3.8) showed a minor $\boldsymbol{y}_2$ ion at *m/z* 438 which indicated loss of a Gly-Ala-Ala b_3 neutral fragment from the straight peptide chain.

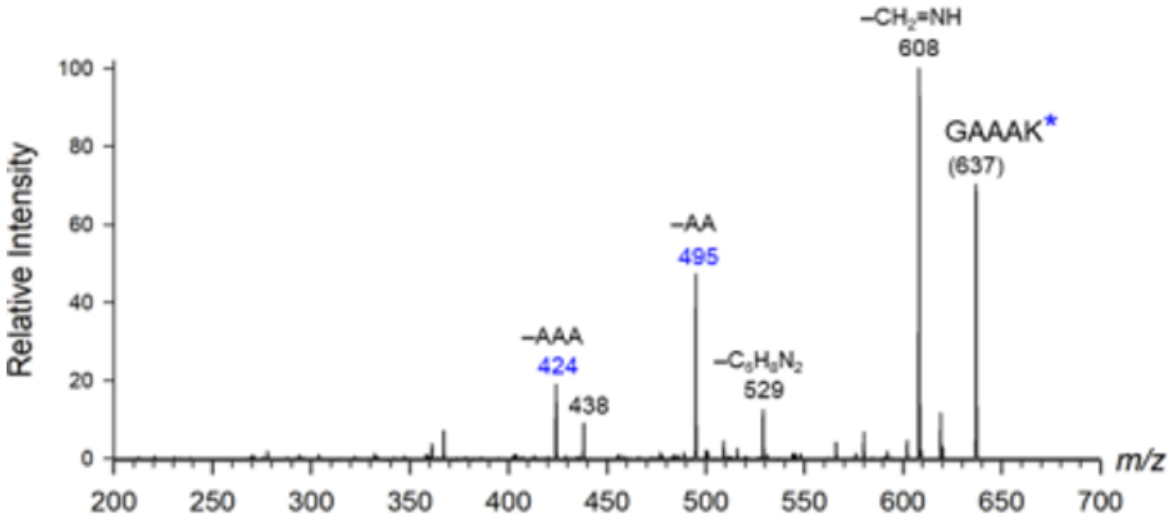

Figure 3. 8. CID-MS^3 spectrum of $(GAAA(tet\text{-}N_2)K + H)^+$ ion.

The CCS_{th} of the protonated nitrile imine isomer **G3** (257.5 $Å^2$) was close to that of the second major peak in the c-IMS arrival time profile. However, isomer **G3** was excluded on the basis of its incompatible absorption spectrum (Figure 3.5c). The low-energy hydrazidine **G4** had a CCS_{th} that did not match any of the experimental values and, in accordance with its nonmatching vibronic spectrum (Figure 3.5d), was excluded. The CCS_{th} of oxadiazole **G5** was at the low end of the CCS_{exp} values; however, its vibronic spectrum (Figure 3.5e) did not match the

action spectrum. The CCS_{th} of hydrazones **G6** (251.3 $Å^2$) and **G7** (241.5 $Å^2$) matched within -1.1% and -1.8%, respectively, the CCS_{exp} of the major peaks from c-IMS. In addition, another conformer of the same type (**G8**) had CCS_{th} = 243 $Å^2$ which was within -1.1% of the CCS_{exp} of the major c-IMS peak. In addition to having closely related CCS, structures **G6**-**G8** also had vibronic spectra that match the major bands in the action spectrum of $(GAAA(tet\text{-}N_2)K + H)^+$. Hence, the combination of c-IMS and UV-vis action spectroscopy provided data that upon analysis allowed us to assign probable structures to the reaction products while excluding those that showed close fits in only one type of experimental data.

Table 3. 1. Calculated relative energies and collision cross sections of $(GAAA(tet\text{-}N_2)K + H)^+$ ions.

ion	relative energy[a,b,c]	CCS[d]
G1	0 (0)	249.6 ± 1.0[e]
G2	13 (19)	245.3 ± 1.2
G3	28 (17)	257.5 ± 1.4
G4	-84 (-65)	231.5 ± 1.0
G5	-67 (-54)	241.3 ± 0.6
G6	-43 (-33)	251.3 ± 1.4
G7	-44 (-30)	241.5 ± 1.0
G8	-32 (-18)	242.9 ± 1.0

[a]In kJ mol^{-1}. [b]From M06-2X/6-311++G(2d,p) single-point energy calculations including zero-point energies and referring to 0 K. [c]Relative Gibbs energies at 310 K in parentheses. [d]In $Å^2$. [e]Standard deviations from multiple runs (n = 10).

The formation of crosslinked structures **G6**-**G8** raised the question of the pertinent reaction mechanism(s). These structures showed the formation of a C=O bond by amide oxygen

transfer to the nitrile imine carbon, and a new C-N bond to the imine nitrogen. We proposed a tentative mechanism that accounts for these changes in (GAAA(*tet*-N_2)K + H)$^+$ which is shown in Figure 3.9. A formal [3+2] addition of the Gly amide to the nitrile imine was presumed to initially form intermediate **3**. This step may be facilitated by proton transfer to the nitrile imine; note that the role of catalytical initial proton transfer was corroborated by the absence of crosslinking in sodium ion adducts (Figure 3.10) that lacked active protons. The protonated oxapyrrazoline ring in **3** presumably opened by breaking the quaternary C-O bond, forming a hydrazide (**4**), which in (GAAA(*tet*-N_2)K + H)$^+$ was finally stabilized by proton migration back to the *N*-terminal amine group, producing conformers **2a**,**2b**. Structures **2a**,**2b** were compatible with the major dissociations of (GAAA(*tet*-N_2)K + H)$^+$ ions upon CID that showed loss of CH_2=NH and $PhNHNH_2$ (Figure 3.8) The final step of proton migration (**4** → **2a,b**) may be reversible, depending on the basicity of the pertinent nitrogen atoms and proton stabilization by hydrogen bonding.

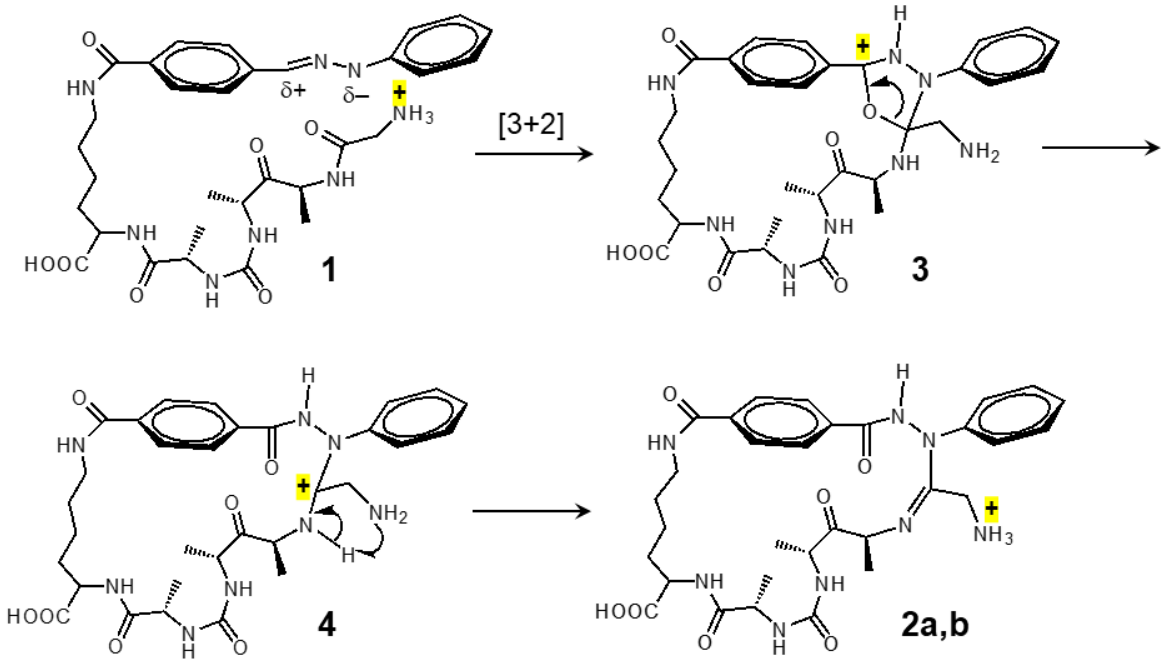

Figure 3. 9. Proposed mechanism for nitrile imine-amide crosslinking.

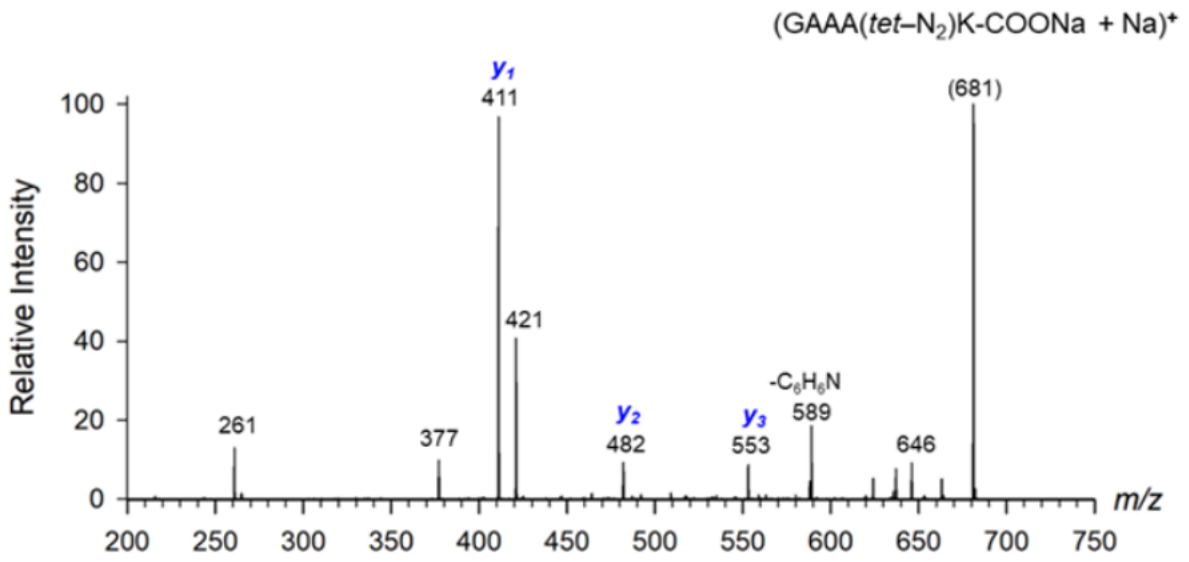

Figure 3. 10. UVPD-CID-MS^3 spectra of (GAAA(*tet*-N_2)K-COONa + Na)$^+$, m/z 681.

To further explore the nitrile-imine reactivity towards other functional groups, we investigated the non-covalent ion complex of dinucleotide 2'-deoxycytidylguanosine (*dCG*) with the GAAAK-*tet* peptide. The singly protonated complex, (*dCG*-GAAAK-*tet* + H)$^+$, was produced by electrospray ionization, selected by mass (*m/z* 1221), and submitted to UVPD. Figure 3.11a shows that efficient (>50%) photodissociation was achieved in 2 laser pulses at 250 nm that triggered loss of N_2 from the tetrazole ring. CID-MS^3 of the mass-selected photoproduct (*m/z* 1193, Figure 3.11b) resulted in a highly selective loss of cytosine (*C*, *m/z* 1082) and dideoxycytidine (*dC*, *m/z* 984) by standard phosphoric ester elimination.[85,86] In contrast, no loss of guanosine was observed, as evidenced by the lack of a *m/z* 944 fragment ion. Only a very minor fraction of (*dCG*-GAAA(*tet*-N_2)K + H)$^+$ underwent dissociation to the components, as documented by the very weak peak of (GAAA(*tet*-N_2)K + H)$^+$ at *m/z* 637 (Figure 3.11b). The spectra can be unequivocally interpreted as evidence for highly efficient and selective nitrile imine crosslinking to the guanine ring. BOMD + DFT calculations of (*dCG*-GAAAK-*tet* + H)$^+$

precursor complexes indicated low-energy structures in which cytosine was protonated at N-3, and the guanine ring was wedged in a loop formed by GAAA(*tet*)K (Figure 3.11a, inset). We note that protonation of free *dCG* favors the guanine N-7 position,[88] so the low energy of cytosine-protonated (*dCG*-GAAAK-*tet* + H)$^+$ must be due to the nucleobase coordination to the tetrazole system. This complex geometry may favor proton transfer to the nitrile imine, followed by addition to the guanine ring. The guanine bonds engaged in the nitrile-imine reaction (C=O, N7-C8, etc.), structures of the crosslink(s), and the mechanism of this new reaction are currently being investigated.

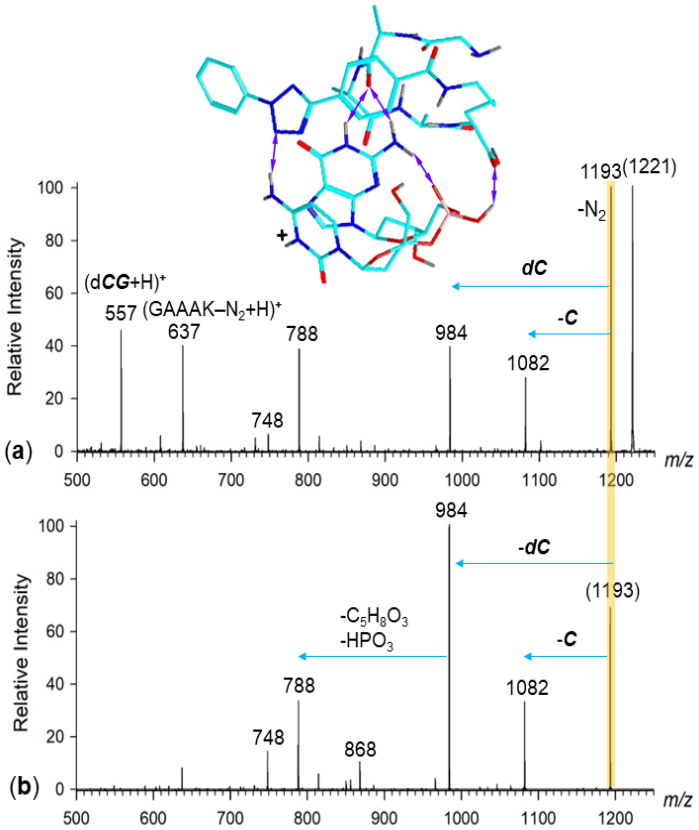

Figure 3. 11. (a) UVPD-MS^2 spectrum of the (*dCG*-GAAA(*tet*)K + H)$^+$ complex. Inset shows the M06-2X/6-31+G(d,p)-optimized structure of a low-energy ion. Only exchangeable hydrogens are shown to avoid clutter. (b) CID-MS^3 spectrum of (*dCG*-GAAA(*tet*-N_2)K + H)$^+$. Hydrogen bonds are visualized by double-headed purple arrows.

3.1.2 *(tet)KAAAG*

Placing the *tet*-tagged at the N-terminus of peptide chain was also performed for more complete vision of gas-phase nitrile imine crosslinking behaviors. As expected, modifications of the N-terminal residues, such as in ((*tet*)KAAAG + H)$^+$, did not affect UVPD, resulting in an efficient loss of N_2 and nitrile imine formation (as shown in Figure 3.12a)

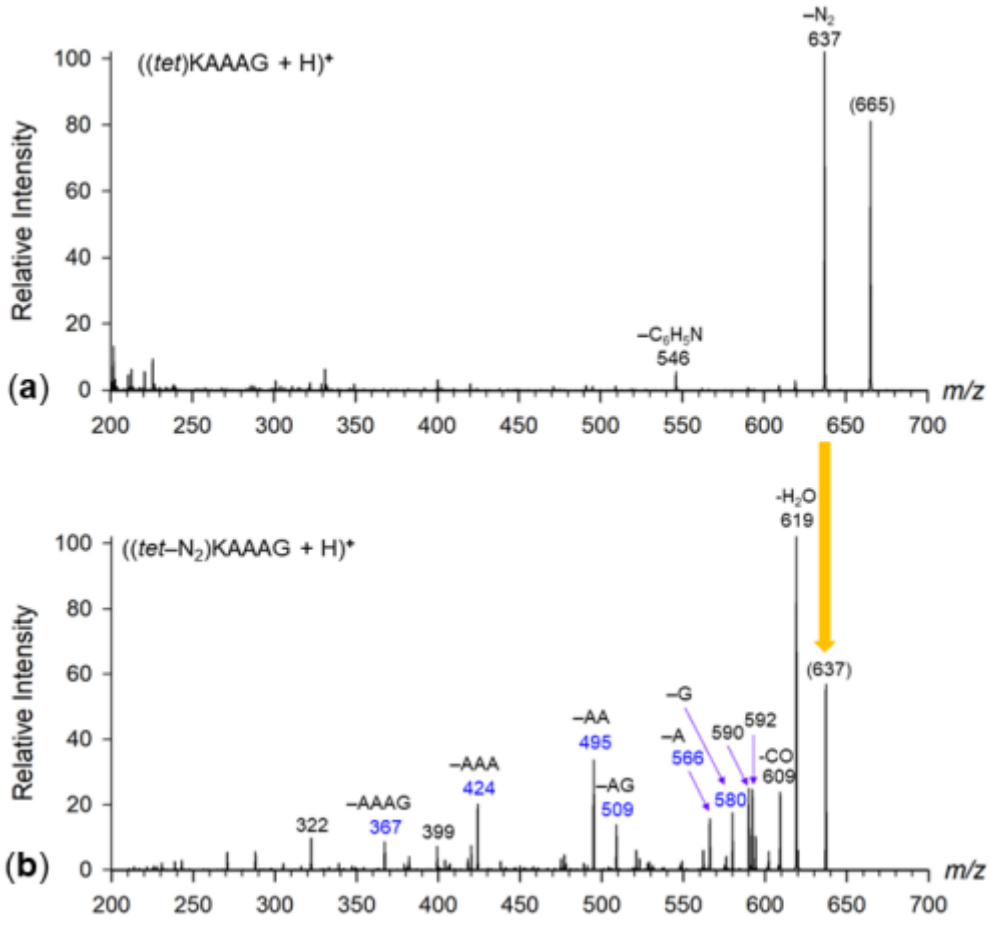

Figure 3. 12. (a) UVPD-MS^2 spectrum, 2 laser pulses at 250 nm, of ((*tet*)KAAAG + H)$^+$, m/z 665, (b) UVPD-CID-MS^3 spectrum of ((*tet*-N_2)KAAAG + H)$^+$, m/z 637.

CID-MS^3 of the inverted sequence ion, ((*tet*-N_2)KAAAG + H)$^+$, showed a major loss of water and internal fragments by loss of Gly, Ala, Ala-Gly, Ala-Ala, and Ala-Ala-Ala (Figure 3.12b) attested to a ring structure formed by nitrile imine crosslinking. Fragment ions of the b_n

type, which are characteristic of glycine C-terminated *N*-linked conjugates,[89] were absent in the CID-MS^3 spectrum of $((tet\text{-}N_2)KAAAG + H)^+$, also indicating nearly complete cyclization involving the glycine residue. In particular, the loss of Gly as $HNCH_2CO$ (57 Da) and Ala-Gly (128 Da) were indicative of a carboxyl linkage to the nitrile imine.

Series of BOMD and DFT calculations of ion structures were performed to establish the structures of $((tet)KAAAG + H)^+$ and its photodissociation products in the gas phase ions. The initial guesses in these calculations comprised nitrile imine protomers and conformers. The lowest-energy structures of $((tet)KAAAG + H)^+$ ion are shown below (Figure 3.13). Due to its basicity, the protonation sites are stable at guanidine position of all structures. **K2** (5 kJ mol^{-1} relative to **K1)** has a similar structure in comparison with **K1**. The other low-energy conformers **K3** (-1.0 kJ mol^{-1} relative to **K1)** and **K4** (-1.6 kJ mol^{-1} relative to **K1)** were considered for further analysis.

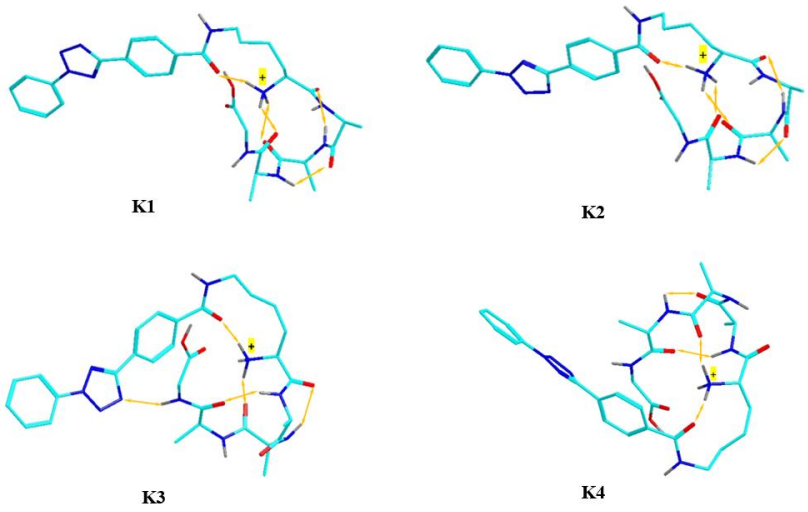

Figure 3. 13. M06-2X/6-31+G(d,p) optimized structures of representative low-energy $((tet)KAAAG + H)^+$ ions **K1**-**K4**. Atom color coding is as follows: cyan = C, blue = N, red = O, gray = H. Only exchangeable hydrogens are shown to avoid clutter. Hydrogen bonds are visualized by double-headed ochre arrows.

From the lowest engergy structure of ((*tet*)KAAAG + H)$^+$ ions, which is determined as **K1**, N_2 were removed to create initial inputs for ((*tet*-N_2)KAAAG + H)$^+$ ions structure calculations. Most optimized structures of the ions are shown in Figure 3.14, with **K5** having lower energy than **K6,** due to its compacted structure**.**

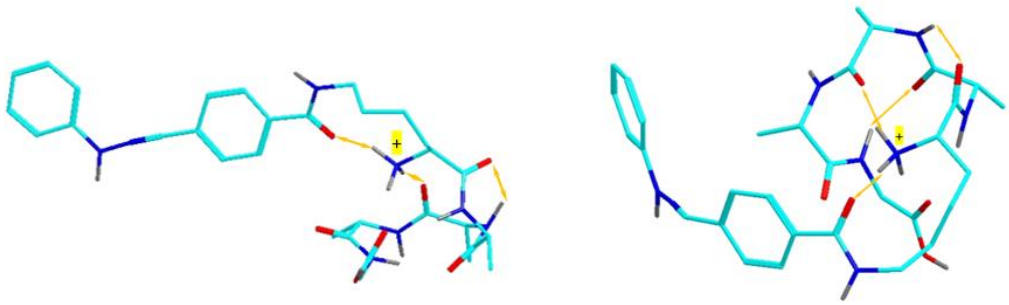

Figure 3. 14. M06-2X/6-31+G(d,p) optimized structures of representative low-energy ((*tet*-N_2)KAAAG + H)$^+$ ions **K5-K6**. Atom color coding is as follows: cyan = C, blue = N, red = O, gray = H. Only exchangeable hydrogens are shown to avoid clutter. Hydrogen bonds are visualized by double-headed ochre arrows.

Additionally, hypothetically cyclized structures involving functional groups were considered, which could potentially produce the major fragment ions in the CID-MS^3 spectrum (Figure 3.15). As mentioned above, carboxyl group of C-terminal of ((*tet*-N_2)KAAAG + H)$^+$ ion was indicated to contribute to cyclization of crosslinking process. Staring with **K5**, as confirmed as the lowest energy structure of ((*tet*-N_2)KAAAG + H)$^+$ ion, input files for BOMD calculations were created. The carboxyl group was moved near to nitrile imine group within a decent distance for C=O bond formation. Figure 3.9, structure 2b, was used as a guide to create the hypothetical cyclized structure. The ion structures maintain +1 charge and singlet configurations.

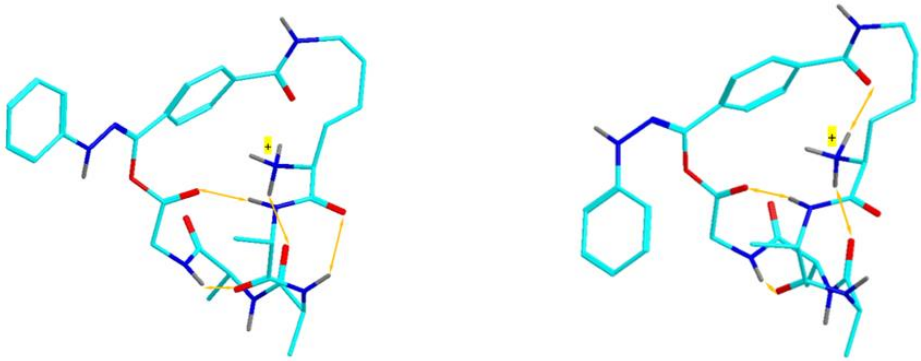

K7 K8

Figure 3. 15. M06-2X/6-31+G(d,p) optimized structures of representative low-energy cyclized ((*tet*-N_2)KAAAG + H)$^+$ ions **K7-K8**. Atom color coding is as follows: cyan = C, blue = N, red = O, gray = H. Only exchangeable hydrogens are shown to avoid clutter. Hydrogen bonds are visualized by double-headed ochre arrows.

In order to have a complete look of crosslinking behaviors of the ((*tet*)KAAAG + H)$^+$ ion in the gas phase, dissociation energies were calculated in shown in Table 3.2 below.

Table 3. 2. Dissociation energy of ((*tet)*KAAAG + H)$^+$ ion from different basis sets.

Reaction	**Dissociation Energies (kJ/mol)**		
	B3LYP+GD3BJ	**M06-2X**	**M06-2X**
	6-31+G(d,p)	***6-31+G(d,p)***	***6-311++G(2d,p)***
K1 → K5 + N_2	47.9	57.2	38.2
K1 → K6 + N_2	49.8	58.6	38.9
K5 → K7	-102.9	-135.2	-130.9
K1 → K7 + N_2	-32.5	-60.0	-78.1
K2 → K7 + N_2	-55.1	-77.9	**-92.7**

Crosslinking to the C-terminal residue, as in ((*tet*-N_2)KAAAG + H)$^+$ may involve simple nucleophilic attack by the carboxyl at the nitrile imine that is promoted by proton transfer. Figure 3.16 indicates that the overall reaction from ((*tet*)KAAAG + H)$^+$ to the cyclized ((*tet*-N_2)KAAAG + H)$^+$ product is substantially exergonic and thus possible following

photodissociation. The conformations of the lowest-energy ((*tet*)KAAAG + H)$^+$ precursor ions in Figure 3.16 allow facile access of the carboxyl proton and oxygen to the nitrile imine for proton transfer and ring closure. The role of the charged *N*-terminal NH_3 group in reversibly providing the proton has not been established and would require extensive transition state search to be elucidated.

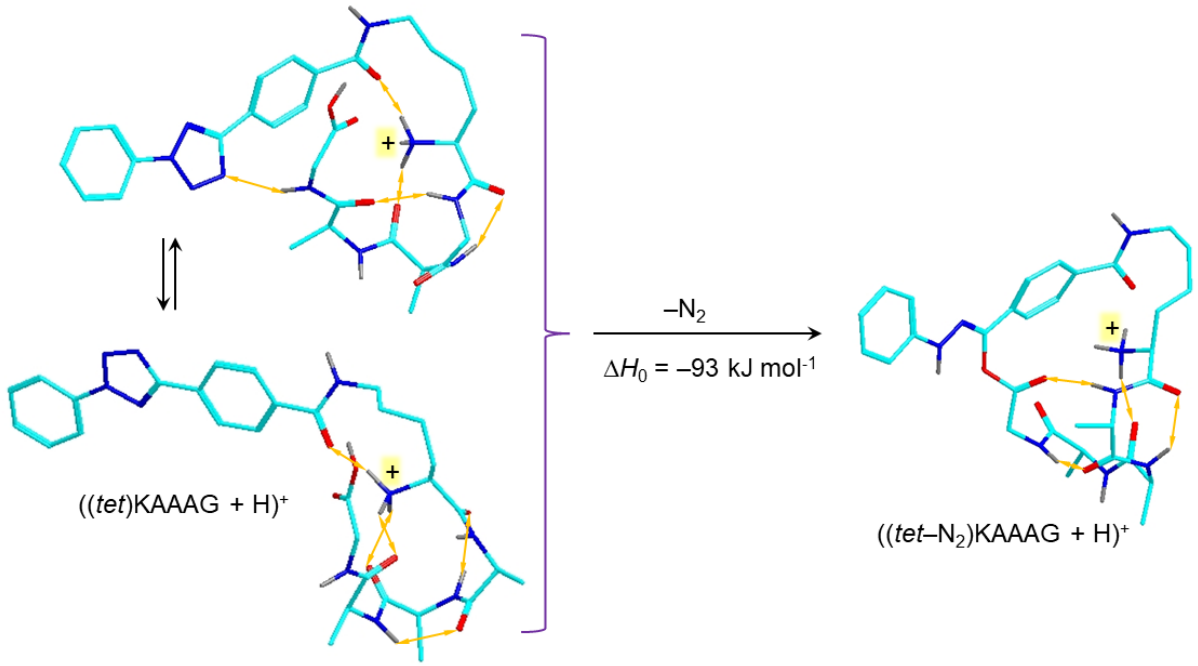

Figure 3. 16. Loss of N_2 and Cyclization in ((*tet*)KAAAG + H)$^+$. The reaction enthalpy is from M06-2X/6-311++G(2d,p) calculations and refers to 0 K.

3.2 Gas-Phase Peptide Ion Scaffolds

Compared to non-covalent complexes, the use of scaffolds for crosslinking studies brings several advantages. First, gas-phase scaffold ions are generated abundantly by electrospray ionization because there are no issues with their stability. Second, products of insertion and elimination are readily distinguished and identified by comparing the CID-MS^3 data of the photoproducts with

those of synthetic standards, such as olefins or macrocyclic lactones. Third, peptide sequence variants, derivatization, and H/D exchange are feasible to be used for mechanistic studies.

The model consists of a trans-4-aminocyclohexane-1-carboxyl scaffold (**1,4-s**) and cis-2-aminocyclohexane-1-carboxyl scaffold (**1,2-s**) that combines the 2,5-diaryltetrazole precursor with the target peptide moiety in one molecule (examples are shown in Figure 3.17). Both the size and composition of the peptide moiety are broadly variable. Here, we used peptide sequences consisting of hydrophobic alanine and glycine residues, as well as those containing a basic side-chain histidine and arginine residues. This way, one can modify peptide protonation sites and affect the peptide chain conformation. The experimental studies are complemented by computational structure analysis. To interpret the results of scaffold photodissociation and nitrile imine cross-linking, extensive calculations of ion structures and dynamics, including BOMD and DFT calculations, have been carried out. The main aims of these calculations were to determine the most energetically favorable protonation sites and ion conformations of the nitrile imine-containing scaffolds and to analyze dynamic between the incipient nitrile imine and peptide bonds in thermal ions.

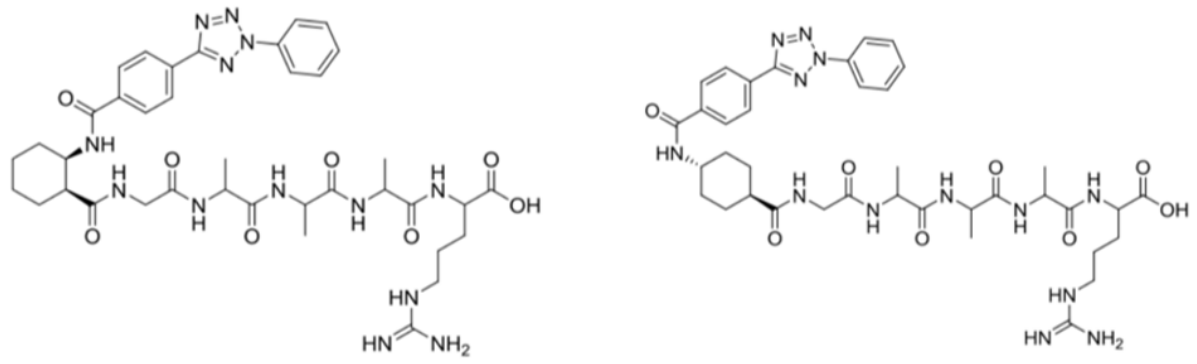

1,2-s-GAAAR 1,4-s-GAAAR

Figure 3. 17. Example scaffold model for nitrile imine crosslink study. GAAAR can be replaced by desired peptide chain.

3.2.1 *Scaffold AAAG*

The chosen ions were protonated at the N-terminus regardless of the initial proton position in structures that were submitted to BOMD. The optimized structures showed globular peptide moieties that were maintained by multiple intramolecular hydrogen bonds. Nevertheless, the Gibbs energy differences among the various protomers and conformers were small enough to allow proton migrations among the amide groups as well as ensuring a conformational mobility of the peptide C-terminus and side chain in thermal ions. In an effort to further characterize the ions of interest, we investigated the composition and structures of the peptide tetrazole conjugates and their crosslinked products using cyclic ion mobility spectrometry (c-IMS).[85] This allowed us to separate isomers by their arrival times and obtain collision cross sections (CCS_{exp}) in N_2. ((*tet*)-1,2-s-AAAG + H)$^+$ ions showed double peaks after four passes (392 cm pathlength) of c-IMS, indicating structurally heterogeneous ions. (Figure 3.18)

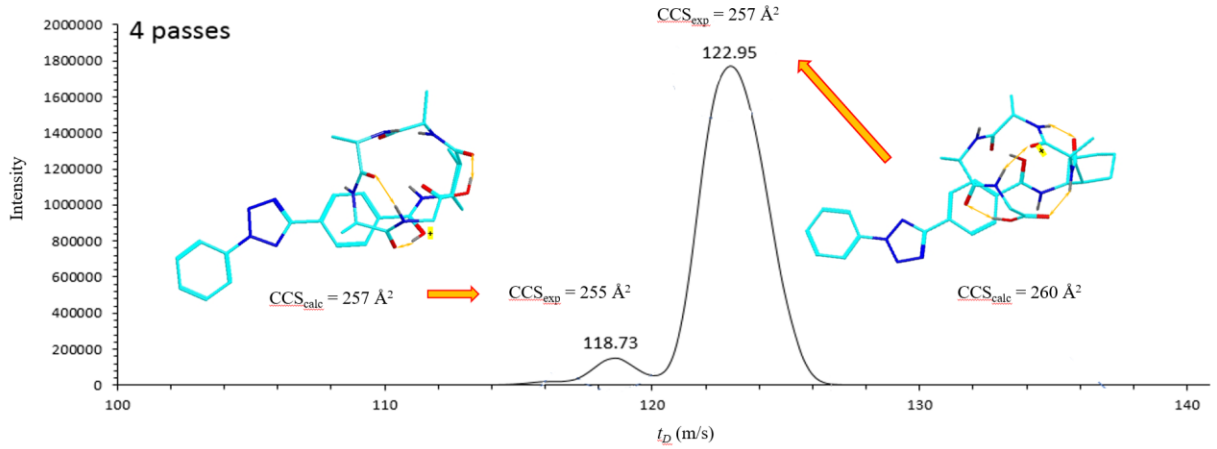

Figure 3. 18. Arrival time profiles (5 cycles), M06-2X/6-31+G(d,p) optimized structures, and CCS values of ((*tet*)-1,2-s-AAAG + H)$^+$ ion

The scaffold structure of the cis-2-aminocyclohexane-1-carboxyl scaffold that combines the 2,5-diaryltetrazole give the flexibility for nitrile imine access amide bonds and other functional groups to perform crosslinking behaviors. From the optimized structures one can assess the minimum number of four residues that separate the tetrazole ring and the incipient nitrile imine from the nearest sterically possible crosslinking site. The gas-phase cations underwent photodissociation at 250 nm, leading to the formation of temporary nitrile imines, which were examined using CID-MS^3 (see Figure 3.19, bottom panel). The resulting spectrum displayed over 90% of fragment ions generated by the elimination of internal peptide residues, indicating peptide cyclization[89,90] to the nitrile imine. This outcome was notably distinct from the dissociations observed in tetrazole-peptide conjugates, which typically exhibited standard sequence ions ($\boldsymbol{b}_n$ and $\boldsymbol{y}_n$ types). Therefore, the formation of internal fragments from the photoproducts served as clear evidence of nitrile imine crosslinking. Structural analysis (refer to Figure 3.19) indicated that only the C-terminal Gly was accessible for reacting with the nitrile

imine group due to steric constraints. The calculated reaction enthalpy for nitrile imine formation via N_2 loss upon absorbing a 250 nm photon (4.96 eV, 479 kJ mol-1), denoted as $\Delta H_{rxn,0}$ = 51 kJ mol^{-1} using M06-2X/6-311++G(2d,p), suggested that the nitrile imine intermediate was generated with significantly elevated internal energy. This excitation energy can be estimated as $E_{exc} \leq 479 - 51 = 428$ kJ mol^{-1}, considering the translational energy of the departing N_2 molecule. The high internal energy from photodissociation is presumed to drive subsequent reactions of the nitrile imine to proceed on the millisecond time scale of the experiment and result in efficient crosslinking, as evidenced by the CID-MS^3 data.

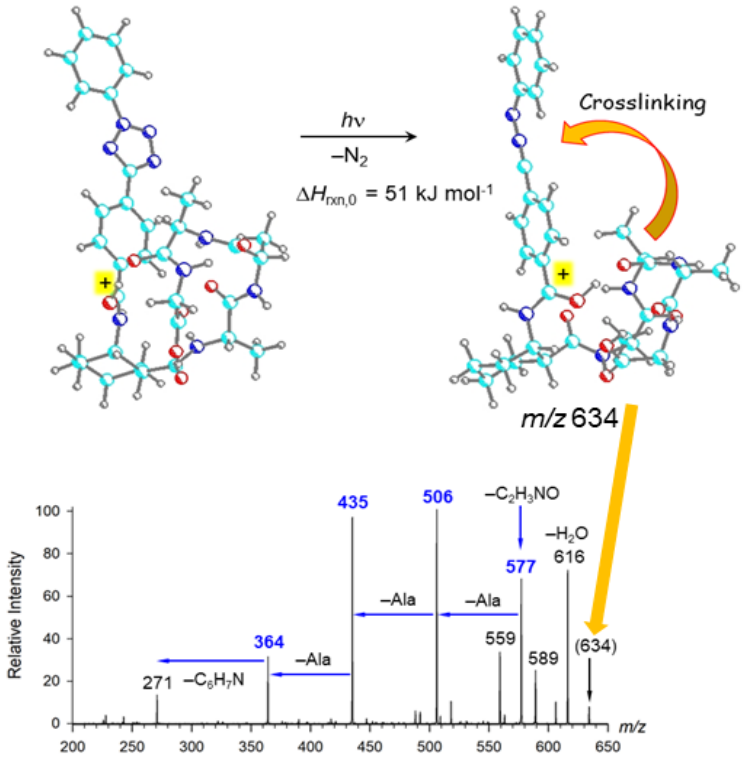

Figure 3. 19. Top: M06-2X/6-31+G(d,p) optimized low energy structures of AAAG-tetrazole scaffold ions. Bottom: UVPD-CID-MS^3 spectrum of the photoproduct after loss of N_2. Blue colored fragment ions indicate crosslinking. The m/z 559 fragment ion (loss of GlyOH) is indicative of an open peptide chain.

3.2.2 *Scaffold GAAAR*

Modifications of the *N*-terminal residues such as in (*tet*)-1,2-s- and (*tet*)-1,4-s-(GAAAR + H)$^+$ did not affect UVPD, resulting in an efficient loss of N_2 and nitrile imine formation in each cases (Figure 3.20a and Figure 3.21a). The CID-MS^3 dissociations showed variations in the relative intensities of fragment ions. Internal fragments by loss of Ala, Ala-Ala, and Ala-Ala-Ala at m/z 545, 491, and 420 (Figure 3.20b and Figure 3.21b), respectively, attested to a ring structure formed by nitrile imine crosslinking.

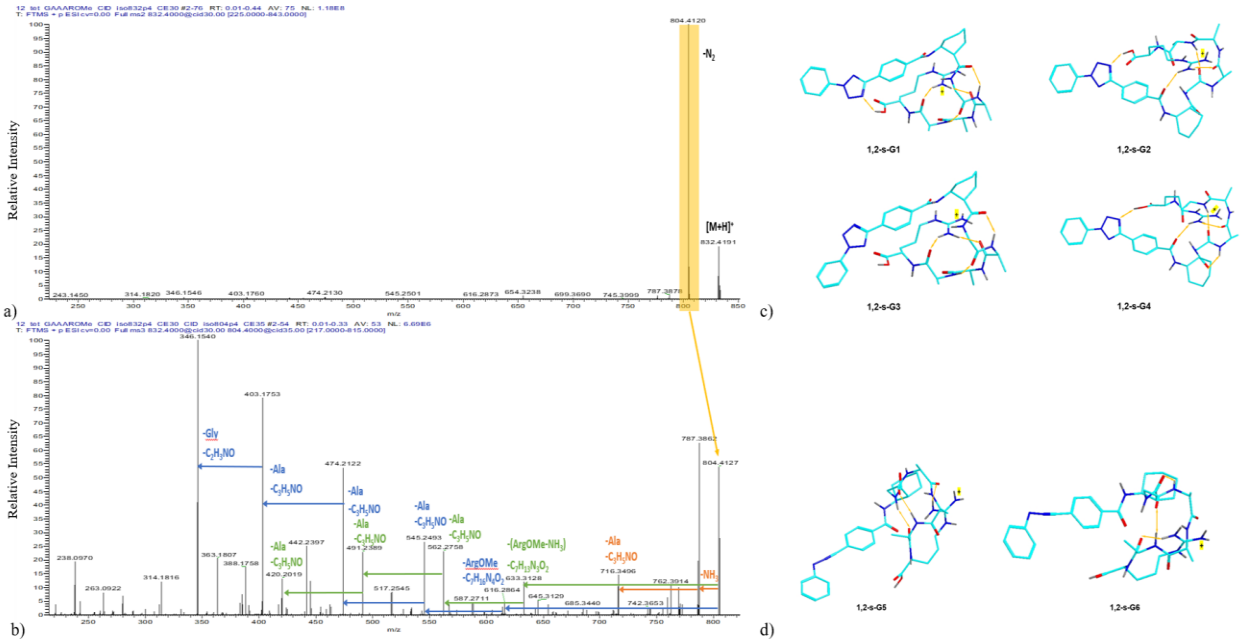

Figure 3. 20. (a) UVPD-MS^2 spectrum of the (*(tet)*-1,2-s-GAAAR + H)$^+$ ion, m/z 832. (b) UVPD-CID-MS^3 spectrum of (*(tet*-N_2*)*-1,2-s-GAAAR + H)$^+$ ion, m/z 804. Hydrogen bonds are visualized by double-headed purple arrows. (c) Set the M06-2X/6-31+G(d,p)-optimized structure of a low-energy ions of precursor. Only exchangeable hydrogens are shown to avoid clutter. (d) Set the M06-2X/6-31+G(d,p)-optimized structure of a low-energy ion of (*(tet*-N_2*)*-1,2-s-GAAAR + H)$^+$. Only exchangeable hydrogens are shown to avoid clutter.

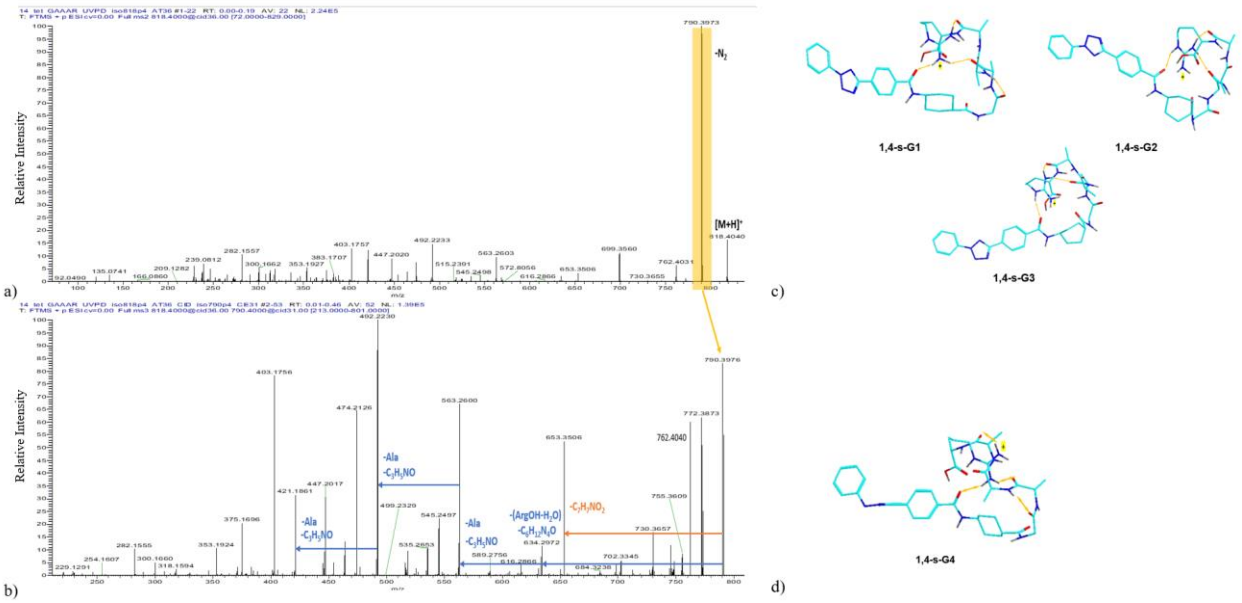

Figure 3. 21. (a) UVPD-MS^2 spectrum of the ((*tet*)-1,4-s-GAAAR + H)$^+$ ion, m/z 832. (b) UVPD-CID-MS^3 spectrum of ((*tet*-N_2)-1,4-s-GAAAR + H)$^+$ ion, m/z 804. Hydrogen bonds are visualized by double-headed purple arrows. (c) Set the M06-2X/6-31+G(d,p)-optimized structure of a low-energy ions of precursor. Only exchangeable hydrogens are shown to avoid clutter. (d) Set the M06-2X/6-31+G(d,p)-optimized structure of a low-energy ion of ((*tet*-N_2)-1,2-s-GAAAR + H)$^+$. Only exchangeable hydrogens are shown to avoid clutter.

The scaffold structure of each case gives the flexibility for nitrile imine access amide bonds and other functional groups to perform crosslinking behaviors. From the optimized structures one can assess the minimum number of four residues that separate the tetrazole ring and the incipient nitrile imine from the nearest sterically possible crosslinking site. The gas-phase cations underwent photodissociation at 213 nm, leading to the formation of temporary nitrile imines, which were examined using UVPD-MS^3 (Figure 3.20d and 3.21d). The modified peptide chains, in this case – with basic amino acid, did not affect UVPD, resulting in an efficient loss of N_2 and nitrile imine formation. Similarly to scaffold AAAG ions, fragment ions

were generated by the elimination of internal peptide residues, which is shown in the resulting spectra, indicating that peptide cyclization to the nitrile imine. This outcome was also notably distinct from the dissociations observed in tetrazole-peptide conjugates, which typically exhibited standard sequence ions ($\boldsymbol{b}_n$ and $\boldsymbol{y}_n$ types). Therefore, the formation of internal fragments from the photoproducts served as clear evidence of nitrile imine crosslinking for basic peptide chains.

Structural analysis of UVPD-CID-MS^3 spectrum of (*(tet*-N_2*)*-1,2-s-GAAAR + H)$^+$ (Figure 3.20b) indicated the C-terminal Arg was accessible for reacting with the nitrile imine group. In addition, guanidine group of Arg was considered as a potential functional for reacting with the nitrile imine group due to its basicity. To investigate the potential cyclization products, BOMD calculation followed by DFT calculations, as described above, were carried out for all cyclized structures involving functional groups that can potentially give rise to the major fragment ions in the UVPD-CID-MS^3 spectra. The lowest-energy structures of each type are shown in Figure 3.22 for (*(tet*-N_2*)*-1,2-s-GAAAR + H)$^+$ and Figure 3.23 for (*(tet*-N_2*)*-1,4-s-GAAAR + H)$^+$. In an effort to further characterize the ions of interest, we are waiting for the c-IMS results to investigate the composition and structures of the peptide tetrazole conjugates and their crosslinked products.

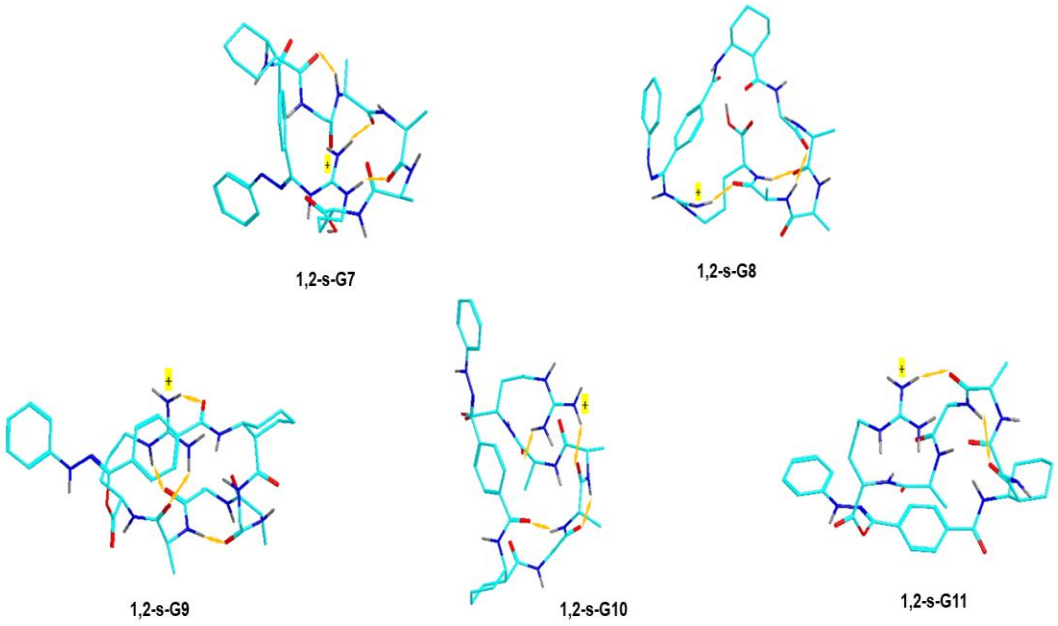

Figure 3. 22. Set the M06-2X/6-31+G(d,p)-optimized structure of a low-energy ion of cyclic ((*tet*-N_2)-1,2-s-GAAAR + H)$^+$. Only exchangeable hydrogens are shown to avoid clutter.

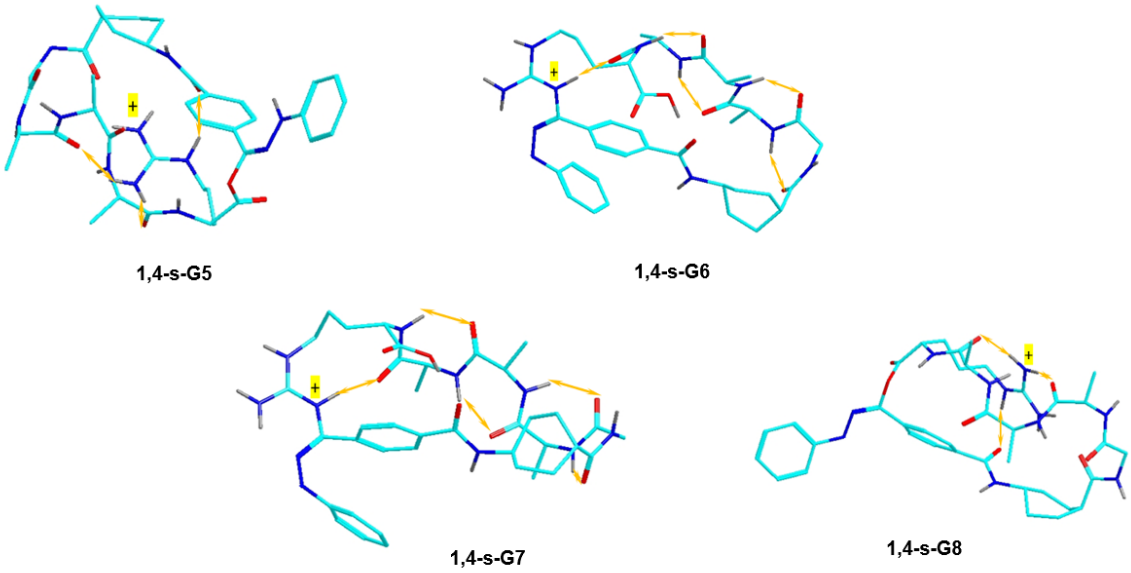

Figure 3. 23. Set the M06-2X/6-31+G(d,p)-optimized structure of a low-energy ion of cyclic ((*tet*-N_2)-1,4-s-GAAAR + H)$^+$. Only exchangeable hydrogens are shown to avoid clutter.

Chapter 4. CONCLUSIONS

Nitrile imine intermediates that were generated from peptide-2,5-diaryltetrazole conjugates have been found to undergo efficient intramolecular cyclization with peptide amide and carboxyl groups. The generation of the nitrile imine intermediates in conjugates can be done efficiently by CID or UVPD at 250 nm. Recently, the wavelength range for photodissociation has been extended to 213 nm UVPD utilizing a laser on a commercially available Thermo Fisher Orbitrap Ascend instrument. However, 250 nm is the preferred wavelength for nitrile imine generation in noncovalent ion complexes which is likely to be the major future application of these novel reactions in gas-phase ions. The role of the amino acid side-chain functional groups and post-translational modifications and their effect on nitrile-imine base crosslinking are the current research directions aimed at exploring the applicability of this new method. Recent findings, including those presented here, suggest that nitrile imine reactions, leading to cyclization and crosslinking, are prevalent in peptide conjugates and have also been observed in non-covalent complexes with nucleotides. Therefore, nitrile imine-based crosslinking of biomolecular ions holds significant potential for exploration and application in biomolecular ion structure analysis. Ongoing research aims to determine the selectivity of functional groups, crosslink structures, and underlying mechanisms involved.

Chapter 5. ACKNOWLEDGEMENTS

Research at the University of Washington was supported by the Chemistry Division of the U.S. National Science Foundation. Additional support by the Klaus and Mary Ann Saegebarth Endowment is gratefully acknowledged.

BIBLIOGRAPHY

1. Jayachandran, B.; Parvin, T. N.; Alam, M. M.; Chanda, K.; & Mm, B. Insights on Chemical Crosslinking Strategies for Proteins. *Molecules* (Basel, Switzerland) **2022**, *27* (23), 8124. https://doi.org/10.3390/molecules27238124
2. Hwang, Y.; Garnelli, J.; Lyubovitsky, J.; Effects of Zero-Length and Non-Zero-Length Cross-Linking Reagents on the Optical Spectral Properties and Structures of Collagen Hydrogels. *ACS Appl. Mater. Interfaces* **2012**, *4* (1), 261-267. https://doi.org/10.1021/am2013147
3. Boutureira, O.; Bernardes, G. J. L.; Advances in Chemical Protein Modification. *Chem. Rev.* **2015**, *115* (5), 2174-2195. https://doi.org/10.1021/cr500399p
4. Trakselis, M. A.; Alley, S. A.; Ishmael, F. T. Identification and Mapping of Protein-Protein Interactions by a Combination of Cross-Linking, Cleavage, and Proteomics. *Bioconjugate Chem.* **2005**, *16* (4), 741-750. https://doi.org/10.1021/bc050043a
5. Gupta, M. N.; Perwez, M. and Sardar, M. Protein Crosslinking: Uses in Chemistry, Biology and Biotechnology. *Biocatalysis and Biotransformation* **2009**, *38* (3), 178-201. https://doi.org/10.1080/10242422.2020.1733990
6. Picchio, M. L.; Linck, Y. G.; Monti, G. A.; Gugliotta, L. M.; Minari, R. J.; Igarzabal, C. I. Casein Films Crosslinked by Tannic Acid for Food Packaging Applications. *Food Hydrocolloids* **2018**, *84*, 424-434. https://doi.org/10.1016/j.foodhyd.2018.06.028
7. Moreno, M. A.; Orgueda, M. E.; Gomez-Mascaraque, L. G.; Isla, M. I.; Lopez-Rubio, A. Crosslinked Electrospun Zein-Based Food Packaging Coatings Containing Bioactive Chilto Fruit Extracts. *Food Hydrocolloids* **2019**, *95*, 495-505. https://doi.org/10.1016/j.foodhyd.2019.05.001

8. Rostom, A. A.; Robinson, C. V. Disassembly of Intact Multiprotein Complexes in the Gas Phase. *Current Opinion in Structural Biology*, **1999**, *9* (1), 135-141. https://doi.org/10.1016/S0959-440X(99)80018-9

9. Hernández, H., Robinson, C. V. Determining the Stoichiometry and Interactions of Macromolecular Assemblies from Mass Spectrometry. *Nat Protoc*, **2007**, *2*, 715-726. https://doi.org/10.1038/nprot.2007.73

10. Gotze, M.; Iacobucci, C.; Ihling, C. H.; Sinz, A. A Simple Cross-Linking/Mass Spectrometry Workflow for Studying System-wide Protein Interactions. *Anal. Chem.* **2009**, *91* (15), 10236-10244. https://doi.org/10.1021/acs.analchem.9b02372

11. Piersimoni, L.; Kastritis, P. L.; Arlt, C.; Sinz, A. Cross-Linking Mass Spectrometry for Investigating Protein Conformations and Protein-Protein Interactions – A Method for All Seasons. *Chem. Rev.* **2022**, *122* (8), 7500-7531. https://doi.org/10.1021/acs.chemrev.1c00786

12. Utrecht, A.Jr.; Makarov, A.; Urlaub, H.; Wysocki, V. Advances in Mass Spectrometry: Unlocking the Potential of Chemical Crosslinking as a Structural Biology Tool. *Drug Target Rev.* **20219.** http://www.drugtargetreview.com/article/53214/advances-in-mass-spectrometry-unlocking-the-potential-of-chemical-crosslinking-as-a-structural-biology-tool.

13. Sinz, A.; Chemical Cross-Linking and Mass Spectrometry for Mapping Three-Dimensional Structures of Proteins and Protein Complexes. *J. Mass Spectrom.* **2003**, *38* (12), 1225-1237. https://doi-org.offcampus.lib.washington.edu/10.1002/jms.559

14. Shigdel, U. K.; Zhang, J.; He, C. Diazirine-Based DNA Photo-Cross-Linking Probes for the Study of Protein-DNA Interactions. *Angew. Chem. Int. Ed*. **2008**, *47* (1), 90-93. https://doi.org/10.1002/anie.200703625

15. Lee, H. S.; Dimla, R. D.; Schultz, P. G. Protein-DNA Photo-Crosslinking with a Genetically Encoded Benzophenone-Containing Amino Acid. *Bioorg. Med. Chem. Let*t. **2009**, *19* (17), 5222-5224. https://doi.org/10.1016/j.bmcl.2009.07.011

16. Turecek, F. Covalent Crosslinking in Gas-Phase Biomolecular Ions. An Account and Perspective. *Phys. Chem. Chem. Phys.* **2023**, *25* (47), 32292-32304. https://doi.org/10.1039/D3CP04879A

17. Singh, A.; Thornton E. R. and Westheimer, F. H. The Photolysis of Diazoacetylchymotrypsin. *J. Biol. Chem.* **1962**, *237* (9), PC3006.

18. Gentry, E. C.; Knowles, R. R. Synthetic Applications of Proton-Coupled Electron Transfer. *Acc. Chem. Res.* **2016**, *49* (8),1546-56. https://doi.org/10.1021/acs.accounts.6b00272

19. Fleet, G. W.; Knowles, J. R.; Porter, R. R. The Antibody Binding Site. Labelling of a Specific Antibody Against the Photo-Precursor of an Aryl Nitrene. *Biochem J.* **1972**, *128* (3), 499-508. https://doi.org/10.1042/bj1280499.

20. Smith, R. A.; Knowles, J. R. Letter: Aryldiazirines. Potential Reagents for Photolabeling of Biological Receptor Sites. *J. Am. Chem. Soc.* **1973**, **95** (15), 5072-5073. https://doi.org/ 10.1021/ja00796a062.

21. Das, J. Aliphatic Diazirines as Photoaffinity Probes for Proteins: Recent Developments. *Chem. Rev.* **2011**, *111* (8), 4405-4417. https://doi.org/10.1021/cr1002722

22. Galardy, R. E.; Craig, L. C.; Jamieson, J. D.; Printz, M. P. Photoaffinity Labeling of Peptide Hormone Binding Sites. *J. Biol. Chem.* **1974**, *249* (11), 3510-3518.

23. Kauer, J. C.; Erickson-Viitanen, S.; Wolfe, H. R. Jr.; DeGrado, W. F. p-Benzoyl-L-Phenylalanine, a New Photoreactive Amino Acid. Photolabeling of Calmodulin with a Synthetic Calmodulin-Binding Peptide. *J. Biol. Chem*. **1986**, *261* (23), 10695-10700.

24. Dorman, G. and Prestwich, G. D. Benzophenone Photophores in Biochemistry. *Biochemistry* **1994**, *33* (19), 5661-5673. https://doi.org/10.1021/bi00185a001

25. Hino, N.; Okazaki, Y.; Kobayashi, T.; Hayashi, A.; Sakamoto, K.; Yokoyama, S. Protein Photo-Cross-Linking in Mammalian Cells by Site-Specific Incorporation of a Photoreactive Amino Acid. *Nat. Meth.* **2005**, *2* (3), 201-206. https://doi.org/10.1038/nmeth739

26. Liu, M. T. H. *Chemistry of Diazirines*; Vol. I and II. CRC Press, Boca Raton **1987**.

27. Frey, H. M and Stevens, I. D. R. The Photolysis of Dimethyldiazerine. *J. Chem. Soc.* **1963**, 3514-3519. https://doi.org/10.1039/JR9630003514

28. Barton, D. H. R.; Jaszberenyi, J. C.; Theodorakis, E. A. and Reibenspies, J. H. The Invention of Radical Reactions. 30. Diazirines as Carbon Radical Traps. Mechanistic Aspects and Synthetic Applications of a Novel and Efficient Amination Process *J. Am. Chem. Soc.* **1993**, *115* (18), 8050-8059. https://doi.org/10.1021/ja00071a017

29. Korneev, S. M. Valence Isomerization between Diazo Compounds and Diazirines. *Eur. J. Org. Chem.* **2011**, *31*, 6153-6175. https://doi.org/10.1002/ejoc.201100224

30. Hashimoto, M.; Hatanaka, Y. Recent Progress in Diazirine-Based Photoaffinity Labeling. *Eur. J. Org. Chem.* **2008**, *15*, 2513-2523. https://doi.org/10.1002/ejoc.200701069

31. Dubinsky, L.; Bastiaan, P. K., Meijler, M. M. Diazirine Based Photoaffinity Labeling. *Bioorg. Med. Chem.* **2012**, *20* (2), 554-570. https://doi.org/10.1016/j.bmc.2011.06.066

32. Kumar, A. B.; Anderson, J. M. and Manetsch, R. Design, Synthesis and Photoactivation Studies of Fluorous Photolabels. *Org. Biomol. Chem.* **2011**, *9* (11), 6284-6292. https://doi.org/10.1039/c1ob05748k

33. Rondan, N. G.; Houk, K. N.; Moss, R. A. Transition States and Selectivities of Singlet Carbene Cycloadditions. *J. Am. Chem. Soc.* **1980**, *102* (6), 1770-1776. https://doi.org/10.1021/ja00526a002

34. Doering, W. von and Knox, L. H. Comparative Reactivity of Methylene, Carbomethoxycarbene and Bis-Carboethoxycarbene toward the Saturated Carbon-Hydrogen Bond. *J. Am. Chem. Soc*. **1961**, *83* (8), 1989-1992. https://doi.org/10.1021/ja01469a050

35. Sakai, S. Theoretical Model for the Reaction Mechanisms of Singlet Carbene Analogs into Unsaturated Hydrocarbon and the Origin of the Activation Barrier. *Int. J. Quant. Chem.* **1998**, *70 (2)*, 291-302. https://doi.org/10.1002/(SICI)1097-461X(1998)70:2<291::AID-QUA5>3.0.CO;2-P

36. Platz, M. S. Atom-Transfer Reactions of Aromatic Carbenes. *Acc. Chem. Res.* **1988**, *21*, 236-242.

37. Mieusset, J. L. and Brinker, U. H. The Carbene Reactivity Surface: A Classification. *J. Org. Chem*. **2008**, *73 (4)*, 1553-1558. https://doi.org/10.1021/jo7026118

38. Senthilnathan, V. P. and Platz, M. S. Determination of the Absolute Rates of Decay of Arylcarbenes in Various Low Temperature Matrixes by Electron Spin Resonance

Spectroscopy. *J. Am. Chem. Soc.* **1980**, *102* (26), 7637-7643. https://doi.org/10.1021/ja00546a003

39. Hadel, L. M.; Maloney, V. M.; Platz, M. S.; McGimpsey, W. G. and Scaiano, J. C. *J. Phys. Chem.* **1986**, *90* (11), 2488-2491. https://doi.org/10.1021/j100402a044
40. Wright, B. B.; Senthilnathan, V. P.; Platz, M. S.; McCurdy, C. W. Jr. Tunneling Parameters for the Hydrogen Atom Abstraction Reactions of Diphenylcarbene in a Low Temperature Toluene Matrix. *Tetrahedron Lett*. **1982**, *23* (8), 833-836. https://doi.org/10.1016/S0040-4039(00)86961-0
41. Shaffer, C. J.; Andrikopoulos, P. C.; Řezáč, J.; Rulíšek, L.; Tureček, F. Efficient Covalent Bond Formation in Gas-Phase Peptide-Peptide Ion Complexes with the Photoleucine Stapler. *J. Am. Soc. Mass Spectrom.* **2016**, *27* (4), 633-645. https://doi.org/10.1007/s13361-016-1338-8
42. Nguyen, H. T. H.; Andrikopoulos, P. C.; Rulíšek, L.; Shaffer C. J.; Tureček, F. Photodissociative Cross-Linking of Non-covalent Peptide-Peptide Ion Complexes in the Gas Phase. *J. Am. Soc. Mass Spectrom.* **2018**, *29*, 1706-1720. https://doi.org/10.1007/s13361-018-1980-4
43. Pepin, R.; Shaffer, C. J.; Tureček, F. Position-Tunable Diazirine Tags for Peptide-Peptide Ion Crosslinking in the Gas-Phase. *J. Mass Spectrom.* **2017**, *52* (8), 557-560. https://doi.org/10.1002/jms.3960
44. Liu, Y.; Ramey, Z.; Tureček, F. Non-Covalent Interactions of a Neuroprotective Peptide Revealed by Photodissociative Cross-Linking in the Gas Phase. *Chem. Eur. J.* **2018**, *24* (37), 9259-9263. https://doi.org/10.1002/chem.201802174

45. Huang, S. R.; Liu Y.; Tureček, F. Non-Covalent Complexes of the Peptide Fragment Gly-Asn-Asn-Gln-Gln-Asn-Tyr in the Gas-Phase. Photodissociative Cross-Linking, Born-Oppenheimer Molecular Dynamics, and Ab Initio Computational Binding Study. *Phys. Chem. Chem. Phys.* **2019**, *21*, 2046-2056. https://doi.org/10.1039/c8cp06893c

46. Nguyen, H. T. H., Huang, S. R., Liu, Y., Liu, Y., Korn, J. A., Turecek, F. Probing Arginine-Phosphopeptide Interactions in Non-Covalent Peptide-Peptide Ion Complexes Using Gas-Phase Cross-Linking and Born-Oppenheimer Molecular Dynamics Calculations. *Int. J. Mass Spectrom*. **2019**, *435*, 259-271. https://doi.org/10.1016/j.ijms.2018.09.037

47. Liu, Y., Tureček, F. Photodissociative Crosslinking of Diazirine-Tagged Peptides with DNA Dinucleotides. *J. Am. Soc. Mass Spectrom.* **2019**, *30* (10), 1992-2006. https://doi.org/10.1007/s13361-019-02189-4

48. Liu, Y.; Liu, Y.; Nytka, M.; Huang, S. R.; Lemr, K. and Turecek, F. Probing d- and l-Adrenaline Binding to β2-Adrenoreceptor Peptide Motifs by Gas-Phase Photodissociation Cross-Linking and Ion Mobility Mass Spectrometry. *J. Am. Soc. Mass Spectrom.* **2021**, *32* (4), 1041-1052. https://doi.org/10.1021/jasms.1c00019

49. Lee, S.; Glover, M. S.; Reilly, J. P.; Clemmer, D. E. Photosynthesis of a combinatorial peptide library in the gas phase. *Anal Chem.* **2015**, *87* (18), 9384-9388. https://doi.org/10.1021/acs.analchem.5b02179

50. McGee; W. M. and McLuckey, S. A. Efficient and Directed Peptide Bond Formation in the Gas Phase via Ion/Ion Reactions *Proc. Natl. Acad. Sci. U. S. A.* **2014**, *111* (4), 1288-1292. https://doi.org/10.1073/pnas.1317914111

51. Kit, M. C. S. and Webb, I. K. Application of Multiple Length Cross-linkers to the Characterization of Gaseous Protein Structure. *Anal. Chem.* **2022**, *94* (39), 13301-13310. https://doi.org/10.1021/acs.analchem.2c03044

52. Huisgen, R.; Seidel, M.; Sauer, J.; McFarland, J., Wallbillich, G. Communications: The Formation of Nitrile Imines in the Thermal Breakdown of 2,5-Disubstituted Tetrazoles. *J. Org. Chem.* **1959**, *24* (6), 892-893. https://doi.org/10.1021/jo01088a034

53. Oh, L. M. Synthesis of Celecoxib via 1,3-Dipolar Cycloaddition. *Tetrahedron Lett*. **2006**, *47* (45), 7943-7946. https://doi.org/10.1016/j.tetlet.2006.08.138

54. Lim, R. K. V and Lin, Q. Photoinducible Bioorthogonal Chemistry: A Spatiotemporally Controllable Tool to Visualize and Perturb Proteins in Live Cells. *Acc. Chem. Res.* **2011**, *44* (9), 828-839. https://doi.org/10.1021/ar200021p

55. Sharp, J. T. Nitrile Ylides and Nitrile Imines. in the Chemistry of Heterocyclic Compounds 59: *Synthetic Applications of 1,3-Dipolar Cycloaddition Chemistry Toward Heterocycles and Natural Products*; Padwa, A., Pearson, W. H., Eds.; John Wiley & Sons: New York, 2002. https://doi.org/10.1002/0471221902.ch7

56. Shawali, A. S. Reactions of Heterocyclic Compounds with Nitrilimines and Their Precursors. *Chem. Rev*. **1993**, *93* (8), 2731-2777. https://doi.org/10.1021/cr00024a007

57. Su, Y. ; Zhao, Y.; Chang, B.; Zhao, X.; Zhang, R.; Liu, X.; Huang, D.; Wang, K.-H.; Huo, C.; Hu, Y. [3 + 2] Cycloaddition of para-Quinone Methides with Nitrile Imines: Approach to Spiro-pyrazoline-cyclohexadienones. *J. Org. Chem.* **2019**, *84* (11), 6719-6728. https://doi.org/10.1021/acs.joc.9b00434

58. Voronin, V. V.; Ledovskaya, M. S.; Gordeev, E. G.; Rodygin, K. S.; Ananikov, V. P. [3 + 2]-Cycloaddition of in Situ Generated Nitrile Imines and Acetylene for Assembling of

1,3-Disubstituted Pyrazoles with Quantitative Deuterium Labeling. *J. Org. Chem.* **2018**, *83* (7), 3819-3828. https://doi.org/10.1021/acs.joc.8b00155

59. Guo, C.-X.; Zhang, W.-Z.; Zhang, N.; Lu, X.-B. 1,3-Dipolar Cycloaddition of Nitrile Imine with Carbon Dioxide: Access to 1,3,4-Oxadiazole-2(3H)-ones. *J. Org. Chem.* **2017**, *82* (14), 7637-7642. https://doi.org/10.1021/acs.joc.7b00963
60. Spiteri, C.; Keeling, S.; Moses, J. E. New Synthesis of 1-Substituted-1H-indazoles via 1,3-Dipolar Cycloaddition of in situ Generated Nitrile Imines and Benzyne. *Org. Lett.* **2010**, *12* (15), 336-83371. https://doi.org/10.1021/ol101150t
61. Tu, L.; Gao, L.; Wang, X.; Shi, R.; Ma, R.; Li, J.; Lan, X.; Zheng, Y; Liu, J. [3 + 2] Cycloaddition of Nitrile Imines with Enamides: An Approach to Functionalized Pyrazolines and Pyrazoles. *J. Org. Chem.* **2021**, *86* (1), 559-573. https://doi.org/10.1021/acs.joc.0c02244
62. Fournier-Le Ray, N.; Joly, N.; Fillaut, J. L. Optimising the Synthesis of 2,5-Diaryltetrazoles: The Decisive Choice of the Reaction Solvent. *Tetrahedron* **2023**, *143*, 133560. https://doi.org/10.1016/j.tet.2023.133560
63. Song, W.; Wang, Y.; Qu, J.; Madden, M. M.; Lin, Q. A Photoinducible 1,3-Dipolar Cycloaddition Reaction for Rapid, Selective Modification of Tetrazole-Containing Proteins. *Angew. Chem. Int Ed. Engl.* **2008**, *47* (15), 2832-2835. https://doi.org/10.1002/anie.200705805
64. Bégué, D.; Qiao, G. G.; Wentrup, C. Nitrile Imines: Matrix Isolation, IR Spectra, Structures, and Rearrangement to Carbodiimides. *J. Am. Chem. Soc*. **2012**, *134* (11), 5339-5350. https://doi.org/10.1021/ja2118442

65. Bégué, D.; Wentrup, C. Carbenic Nittrile Imines: Properties and Reactivity. *J. Org. Chem.* **2014**, *79* (3), 1418-1426. https://doi.org/10.1021/jo402875c

66. Marshall, D. L.; Menzel, J. P.; McKinnon, B. I.; Blinco, J. P.; Trevitt, A. J.; Barner-Kowollik, C. and Blanksby, S. J. Laser Photodissociation Action Spectroscopy for the Wavelength-Dependent Evaluation of Photoligation Reactions. *Anal. Chem.* **2021**, *93* (22), 8091-8098. https://doi.org/10.1021/acs.analchem.1c01584

67. Moriwaki, Y.; Tachikawa, M.; Maeno, Y.; Shimizu, T. Collision Cooling of Ions Stored in Quadrupole Radio-Frequency Trap. *Jpn. J. Appl. Phys.* **1992**, *31* (11), 1640-1643. https://doi.org/10.1143/jjap.31.l1640

68. Pepin, R.; Tureček, F. Kinetic Ion Thermometers for Electron Transfer Dissociation. *J. Phys. Chem. B*, **2015**, 119 (7), 2818-2826. https://doi.org/10.1021/jp510244d

69. Řezáč, J.; Fanfrlik, J.; Salahub, D.; Hobza, P. Semiempirical Quantum Chemical PM6 Method Augmented by Dispersion and H Bonding Correction Terms Reliably Describes Various Types of Noncovalent Complexes. *J. Chem. Theory Comput.* **2009**, *5* (7), 1749-1760. https://doi.org/10.1021/ct9000922

70. Řezáč, J. Cuby: An Integrative Framework for Computational Chemistry. *J. Comput. Chem.* **2016**, *37* (13), 1230-1237. https://doi.org/10.1002/jcc.24312

71. Berendsen, H. J. C.; Postma, J. P. M.; van Gunsteren, W. F.; DiNola, A.; Haak, J. R. Molecular Dynamics with Coupling to an External Bath. *J. Chem. Phys.* 1**984**, *81*, 3684-3690. https://doi.org/10.1063/1.448118

72. Stewart, J. J. P. *MOPAC 16*; Stewart Computational Chemistry: 2016.

73. Becke, A. D. Density-Functional Exchange-Energy Approximation with Correct Asymptotic Behavior. *Phys. Rev. A* **1988**, *38* (6), 3098-3100. https://doi.org/10.1103/physreva.38.3098

74. Grimme, S.; Ehrlich, S.; Goerigk, L. Effect of the Damping Function in Dispersion Corrected Density Functional Theory. *J. Comput. Chem.* **2011**, *32* (7), 1456-1465. https://doi.org/10.1002/jcc.21759

75. Nickerson, C. J.; Bryenton, K. R.; Price, A. J. A.; Johnson, E. R. Comparison of Density-Functional Theory Dispersion Corrections for the DES15K Database. *J. Phys. Chem. A* **2023**, *127* (41), 8712-8722. https://doi.org/10.1021/acs.jpca.3c04332

76. Zhao, Y.; Truhlar, D. G. The M06 Suite of Density Functionals for Main Group Thermochemistry, Thermochemical Kinetics, Noncovalent Interactions, Excited States, and Transition Elements: Two New Functionals and Systematic Testing of Four M06-Class Functionals and 12 Other Functionals. *Theor. Chem. Acc.* 2008, *120*, 215-241. https://doi.org/10.1007/s00214-007-0310-x

77. Singh, U. C.; Kollman, P. A. An Approach to Computing Electrostatic Charges for Molecules. *J. Comput. Chem.* **1984**, *5* (2), 129-145. https://doi.org/10.1002/jcc.540050204

78. Besler, B. H.; Merz, K. M., Jr., Kollman, P. Atomic Charges Derived from Semiempirical Methods. *J. Comput. Chem.* **1990**, *11* (4), 431-439. http://doi.org/10.1002/jcc.540110404

79. Ieritano, C.; Crouse, J.; Campbell, J. L.; Hopkins, W. S. A Parallelized Molecular Collision Cross Section Package with Optimized Accuracy and Efficiency. *Analyst* **2019**, *144*, 1660-1670. https://doi.org/10.1039/c8an02150c

80. Ieritano, C.; Hopkins, W. S. Assessing Collision Cross Section Calculations Using MobCal-MPI with a Variety of Commonly Used Computational Methods. *Mater. Today Commun*. **2021**, *27*, 102226. https://doi.org/10.1016/j.mtcomm.2021.102226

81. Furche, F.; Ahlrichs, R. Adiabatic Time-Dependent Density Functional Methods for Excited State Properties. *J. Chem. Phys.* **2002**, *117* (16), 7433-7447. https://doi.org/10.1063/1.1508368

82. Wigner, E. On The Quantum Correction for Thermodynamic Equilibrium. *Phys. Rev.* **1932**, *40* (5), 749-759. https://doi.org/10.1103/physrev.40.749

83. Bonacic-Koutecky, V.; Mitric, R. Theoretical Exploration of Ultrafast Dynamics in Atomic Clusters: Analysis and Control. *Chem. Rev.* **2005**, *105* (1), 11-66. https://doi.org/10.1021/cr0206925

84. Barbatti, M.; Ruckenbauer, M.; Plasser, F.; Pittner, J.; Granucci, G.; Persico, M.; Lischka, H. Newton-X: A Surface-Hopping Program for Nonadiabatic Molecular Dynamics. Wiley Interdiscip. *Rev. Comput. Mol. Sci.* **2014**, *4* (1), 26-33. https://doi.org/10.1002/wcms.1158

85. Giles, K.; Ujma, J.; Wildgoose, J.; Pringle, S.; Richardson, K.; Langridge, D.; Green, M. A Cyclic Ion Mobility-Mass Spectrometry System. *Anal. Chem.* **2019**, *91* (13), 8564-8573. https://doi.org/10.1021/acs.analchem.9b01838

86. Vrkic, A. K.; O'Hair, R. A. J.; Foote, S, Reid, G. E. Fragmentation Reactions of all 64 Protonated Trimer Oligonucleotides and 16 Mixed Base Tetramer Oligodeoxynucleotides Via Tandem Mass spectrometry in an Ion Trap. *Int. J. Mass Spectrom.* **2000**, *194* (2-3), 145-164. https://doi.org/10.1016/S1387-3806(99)00150-5

87. Wan, J.; Brož, B.; Liu, Y.; Huang, S. R.; Marek, A.; Tureček, F. Resolution of Identity in Gas-Phase Dissociations of Mono- and Diprotonated Trinucleotide Codons by ^{15}N-Labeling and Computational Structure Analysis. *J. Am. Soc. Mass Spectrom.* **2022**, *33* (10), 1936-1950. https://doi.org/10.1021/jasms.2c00194

88. Liu, Y.; Korn, J. A.; Dang, A.; Turecek, F. Hydrogen-Rich Cation Radicals of DNA Dinucleotides. Generation and Structure Elucidation by UV-Vis Action Spectroscopy. *J. Phys Chem. B* **2018**, *122* (42), 9665-9680. https://doi.org/10.1021/acs.jpcb.8b07925

89. Zhu, H.; Zima, V.; Ding, E.; Tureček, F. Carbene Crosslinking in Gas-Phase Peptide Ion Scaffolds. *J. Am. Soc. Mass Spectrom.* **2023**, *34* (4), 763-774. https://doi.org/10.1021/jasms.3c00023

90. Bleiholder, C.; Osburn, S.; Williams, T.; Suhai, S.; Van Stipdonk, M.; Harrison, A.; Paizs, B. *J. Am. Chem. Soc.* **2008**, *130* (52), 17774-17789. https://doi.org/10.1021/ja805074d

91. Novák, J.; Lemr, K.; Schug, K. A.; Havlíček, V. CycloBranch: De Novo Sequencing of Nonribosomal Peptides from Accurate Product Ion Mass Spectra. *J. Am. Soc. Mass Spectrom.* **2015**, *26* (10), 1780-1786. https://doi.org/10.1007/s13361-015-1211-1